Kondo resonance peak in the photoemission spectra of $YbAgCu_4$

H. Anzai[a], R. Tawara[a], Y. Kikuchi[a], H. Sato[b], M. Arita[b],
R. Takaaze[c], K. T. Matsumoto[c], and K. Hiraoka[c]

[a] *Graduate School of Engineering, Osaka Prefecture University, Sakai 599-8531, Japan*
[b] *Hiroshima Synchrotron Radiation Center, Hiroshima University, Higashi-Hiroshima 739-0046, Japan*
[c] *Graduate School of Science and Engineering, Ehime University, Matsuyama 790-8577, Japan*

Keywords: *c-f* hybridization, Yb compound, photoemission spectroscopy.

In the research on rare-earth intermetallic compounds, the interaction between the conduction electrons and the 4*f* electrons (*c-f* hybridization) is one of the intriguing subjects. The *c-f* hybridization produces a large density of states (Kondo resonance) near the Fermi energy, E_F, in the electronic excitation spectrum [1]. This resonance state is due to the formation of Kondo singlet where the local magnetic moment of the 4*f* electron is screened by the collective conduction electrons. A logarithmic increase in electrical resistivity, $\rho(T) \propto -\ln(T)$, below the single-ion Kondo temperature, T_K, appears as a characteristic of a loss of the local magnetic moment [2].

In Kondo lattice where the local moments are periodically arranged, intersite interactions between 4*f* electrons develop with decreasing temperature and form a coherent state with large effective electron masses [3]. This coherent heavy-fermion state gives rise to a reduction in the resistivity at low temperatures [4]. The transport lattice coherence temperature T^* is defined as the maximum in the resistivity and departs from the single-ion Kondo temperature, $T^* < T_K$.

Here, we report a high-resolution photoemission study of the Kondo resonance in the Kondo lattice system $YbAgCu_4$. The linear coefficient of specific heat is a large value of $\gamma = 243$ mJ/mol·K^2, indicating heavy effective masses of 4*f* electrons [5]. The temperature dependence of electrical resistivity exhibits a maximum at $T^* \sim 70$ K, and the drop in $\rho(T)$ at lower temperatures is due to the formation of the coherent heavy-fermion state [5]. The experiments were performed at BL-7 and BL-9A of the Hiroshima Synchrotron Radiation Center.

Figure 1(a) shows the temperature dependence of the $4f_{7/2}$ peak. The peak intensity increases with decreasing temperature. The enhancement of the peak intensity is basically consistent with the predictions of the single impurity Anderson model and the Anderson lattice model [1]. The peak shifts to E_F with decreasing temperature and possibly stops dispersing at low temperatures, as shown by photoemission spectra with a constant offset in Fig. 1(c). We have determined the energy of the $4f_{7/2}$ peak and plotted them as a function of temperature in Fig. 1(e). The peak energy linearly decreases with decreasing temperature from $T = 230$ to 80 K and remains almost unchanged below $T \sim 60$ K. Such a dispersive feature is a characteristic of the Kondo peak in the Anderson lattice model [6]. The dashed line in Fig. 1(e) represents the linear extrapolation from the high-temperature data to the zero-temperature limit. The extrapolated value of 26 meV is in agreement with the energy scale of $T_K \simeq 100$ K.

To quantify the spectral weight of the $4f_{7/2}$ state, we have subtracted the intensity at $T = 230$ K from that at each temperature. This method effectively normalizes the incoherent background contribution on the photoemission spectra and provides a clear view of temperature evolution of the $4f_{7/2}$ peak. As shown by the difference spectra, $I(T) - I(230\text{ K})$, in Fig. 1(b), the intensity of the background-subtracted peak increases with decreasing temperature. Figure 1(d) shows the difference spectra with a constant offset. The colored area represents the spectral weight of the $4f_{7/2}$ peak. We have determined the low-energy spectral weight, W_{LE}, by integrating the intensity over the energy window of the colored area in Fig. 1(d). It is noted that W_{LE} reflects mainly the development of the $4f_{7/2}$ peak, because the background-subtracted intensity of the shoulder structure at $|\omega| \simeq 0.2$ eV is insensitive to temperature. The temperature dependence of W_{LE} as a percentage of the total weight at $T = 10$ K is displayed in Fig. 1(f). As temperature decreases, W_{LE} increases and then forms a plateau below $T \simeq 60$ K. The onset

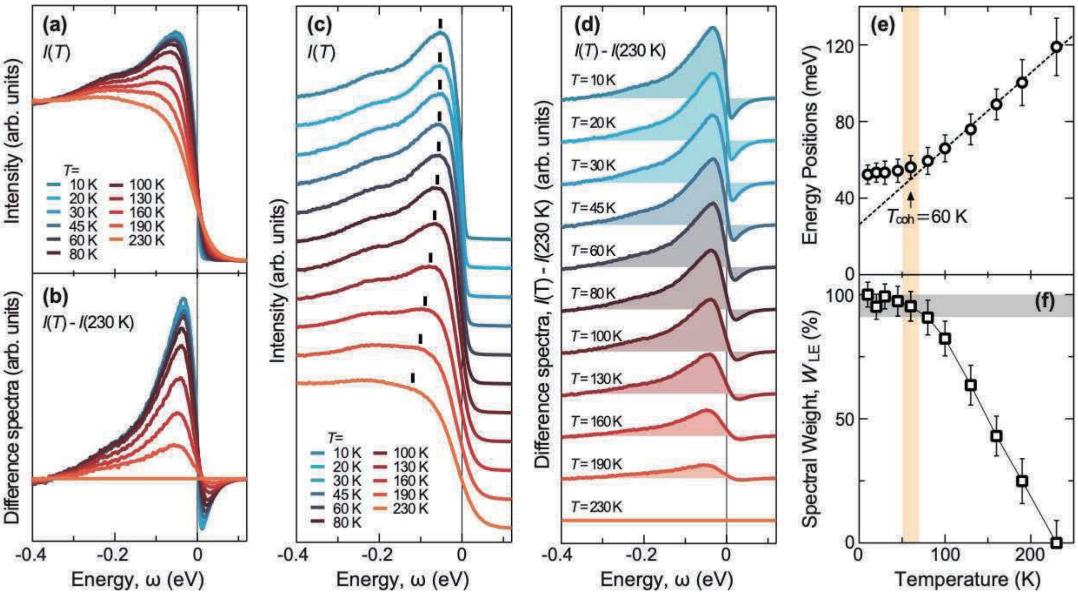

Figure 1. (a) Temperature dependence of photoemission spectra of $4f_{7/2}$ peak, $I(T)$ in $YbAgCu_4$. (b) Difference spectra obtained by subtracting the intensity at $T = 230$ K from that at each temperature, $I(T)$ - $I(230$ K). (c) Same data as in panel (a) and are vertically offset for clarity. The vertical bars denote the energy positions of the $4f_{7/2}$ peak. (d) Same data as in panel (b) and are vertically offset for clarity. The colored area indicates the low-energy spectral weight, W_{LE}. (e) Temperature dependence of the energy of the $4f_{7/2}$ peak. The dashed line indicates a linear extrapolation of data from $T = 80$ to 230 K. (f) Temperature dependence of low-energy spectral weight W_{LE}, which is determined by the integration of intensity over the colored area of the difference spectra in panel (d). The spectral weight is plotted as a percentage of the total weight at $T = 10$ K. The error bars derived from statical and reflected by noise in the data.

temperature of the plateau in W_{LE} is quantitatively similar to that in the peak energy, as shown in Fig. 1(e). This similarity demonstrates that our observations reflect the intrinsic electronic structure of $YbAgCu_4$.

It is noteworthy that the characteristic temperature of $T \simeq 60$ K is comparable to the transport lattice coherence temperature of $T^* \sim 70$ K. This consistency indicates a crossover between the two regimes of the Kondo screening at the higher scale T_{K} and the coherent screening at the lower scale T^*. In the following, we use the notation T_{coh} as the spectroscopic defined coherent temperature. Previous photoemission study has revealed that the large spectral weight for $X = \mathrm{Mg}$ is maintained at $T_{\mathrm{coh}} = 122$ K [7]. Moreover, T_{K} for $X = \mathrm{Mg}$ is ten times larger than that for $X = \mathrm{Ag}$. We assume that T_{coh} is linked to the robustness of the Kondo lattice state. The two relevant energy scales of T_{coh} and T_{K} in the heavy-fermion compounds are consistent with the protracted screening behavior predicted by the Anderson lattice model [6].

REFERENCES

1. R. I. R. Blyth, J. J. Joyce, A. J. Arko, P. C. Canfield, A. B. Andrews, Z. Fisk, J. D. Thompson, R. J. Bartlett, P. Riseborough, J. Tang, and J. M. Lawrence, Phys. Rev. B **48**, 9497 (1993).
2. J. Kondo, Prog. Theor. Phys. **32**, 37 (1964).
3. P. Fulde, Springer Series in Solid-State Sciences Vol. 100 (Springer, Berlin, 1995).
4. M Lavagna, C Lacroix, and M Cyrot, J. Phys. **12**, 745 (1982).
5. J. L. Sarrao, C. D. Immer, C. L. Benton, Z. Fisk, J. M. Lawrence, D. Mandrus and J. D. Thompson, Phys. Rev. B **54**, 12207 (1996).
6. A. N. Tahvildar-Zadeh, M. Jarrell, and J. K. Freer-icks, Phys. Rev. Lett. **80**, 5168 (1998).
7. H. Anzai, S. Ishihara, H. Shiono, K. Morikawa, T. Iwazumi, H. Sato, T. Zhuang, K. T. Matsumoto, and K. Hiraoka, Phys. Rev. B **100**, 245124 (2019).

Electronic Structures and Chemical Natures of Inhomogeneous Gd-TM (TM = Co, Ni, and Cu) Metallic Glasses

Shinya Hosokawa,[a] Jens R. Stellhorn,[b] Hitoshi Sato,[c] Jing Jiang,[d] and Hidemi Kato[d]

[a] *Department of Physics, Kumamoto University, Kumamoto 860-8555, Japan*
[b] *Department of Applied Chemistry, Hiroshima University, Higashi-Hiroshima 739-8527, Japan*
[c] *Hiroshima Synchrotron Radiation Center, Hiroshima University, Higashi-Hiroshima, 739-0046, Japan*
[d] *Institute for Materials Research, Tohoku University, Sendai 980-8577, Japan*

Keywords: Metallic glasses, Thermal rejuvenation effect, Heterogeneity, Chemical nature.

Recently, Ketov *et al.* [1] proposed a new type of the rejuvenation effect in metallic glasses, *i.e.*, a relaxation to a higher energy state, by a thermal cycle. According to their interpretation, if a glass is not elastically homogeneous, the thermal expansion coefficient has a distribution over the glass sample. By repeated temperature changes, magnitudes of thermal expansions are different depending on the positions in the glass, which surely induces shearing forces, and as a result, a rejuvenation effect occurs in the glass. They named this phenomenon as "Rejuvenation of metallic glasses by non-affine thermal strain". The validity of this logic is the subject to the discussion.

Yamazaki [2] intensively studied β-relaxation peaks in Gd-TM (TM = Co, Ni, and Cu) glasses. The β-peaks are remarkably larger than those of other metallic glasses, and thus, large heterogeneities are expected in these glasses. He also found that the heterogeneities highly depend on the transition metal elements, *i.e.,* Ni > Co > Cu.

In order to clarify the structural changes by the rejuvenation effect, we measured high-energy x-ray diffraction measurements. The rejuvenation of the glass samples was made by a thermal cycling between the liquid N_2 and room temperatures 40 times. The obtained pair distribution functions, $g(r)$, have two distinct peaks, where the shorter and longer ones (0.29 and 0.35 nm) correspond to the Gd-TM and Gd-Gd correlations, respectively. After the thermal treatments, slight decreases and distance shifts are observed in these peaks. We also performed anomalous x-ray scattering experiments to further investigate partial structures relating to the rejuvenation effect.

In this study, we start to investigate this thermal rejuvenation effect from another point of electronic views. We have recently measured valence-band and core-level photoemission spectroscopy (PES) on these metallic glasses *before the thermal treatments*.

The amorphous samples were prepared by melt spinning with a single Cu roll installed at the Institute for Materials Research, Tohoku University, Sendai, Japan. Ribbon samples with a thickness of about 20 μm and a width of ~ 2 mm were obtained.

The PES experiments were carried out by using a PES spectrometer installed at the beamline BL7 at Hiroshima Synchrotron Radiation Center in Hiroshima University, Higashi-Hiroshima, Japan. Ultraviolet photons generated from the HiSOR storage ring with the ring energy of 700 MeV and the ring current of 160-300 mA were monochromatized with a Dragon-type monochromator, covering the incident photon energy, $h\nu$, values from 20 to 450 eV. A PES spectrometer with a hemi-spherical photoelectron energy-analyzer (GAMMA-DATA, SCIENTA SES2002) attached to the analyzer chamber under the ultrahigh vacuum below 1×10^{-8} Pa at the end-station, was used for the PES experiments. The overall energy resolution, ΔE, of the spectrometer was about 0.1-0.5 eV depending on the $h\nu$ values of 20-450 eV. The details of the PES experimental setup are given elsewhere [3].

All the PES spectra were collected at room temperature. Clean surfaces were *in situ* obtained by sputtering the samples with Ar^+ ions in a sample preparation chamber with the base pressure below 1×10^{-8} Pa. The energies of all spectra were defined with respect to the Fermi energy, E_F, of the sample or a freshly evaporated Au film.

Figure 1 shows the Gd 4*d* core-level PES spectra of (a) Gd-Ni, (b) Gd-Co, and (c) Gd-Cu glassy alloys. As clearly seen in the figures by arrows, the Gd 4*d* core levels have at least two doublets of $4d_{3/2}$ and $4d_{5/2}$ levels, indicating that the Gd atoms have at least two chemical sites. In the near future, we will detect the spectral changes after the thermal treatments.

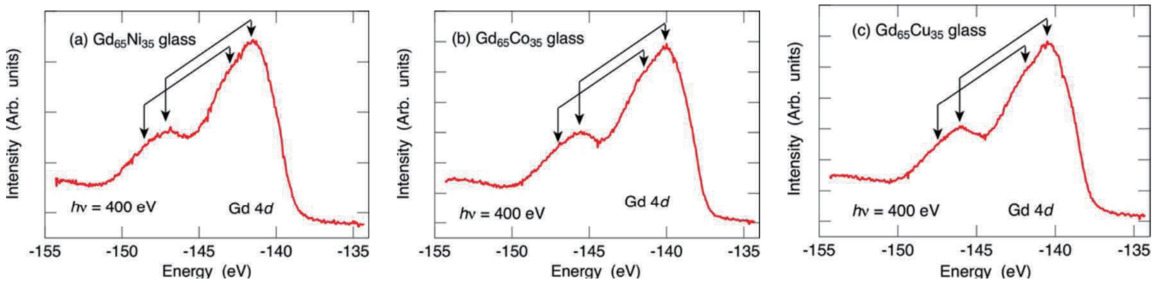

FIGURE 1. The Gd 4*d* core-level PES spectra of (a) Gd-Ni, (b) Gd-Co, and (c) Gd-Cu glassy alloys.

REFERENCES

1. S. V. Ketov, Y. H. Sun, S. Nachum, Z. Lu, A. Checchi, A. R. Beraldin, H. Y. Bai, W. H. Wang, D. V. Louzguine-Luzgin, M. A. Carpenter, and A. L. Greer, *Nature* **524**, 200-203 (2015).
2. Y. Yamazaki, *Thesis* (Tohoku University, 2016).
3. M. Taniguchi and J. Ghijsen, *J. Sync. Rad.* **5**, 1176-1179 (1998).

Conduction-Band Electronic States of Gd-TM Metallic Glass Alloys Having Thermal Rejuvenation Effect

Shinya Hosokawa,[a] Jens R. Stellhorn,[b] Hitoshi Sato,[c] Jing Jiang,[d] and Hidemi Kato[d]

[a] *Department of Physics, Kumamoto University, Kumamoto 860-8555, Japan*
[b] *Department of Applied Chemistry, Hiroshima University, Higashi-Hiroshima 739-8527, Japan*
[c] *Hiroshima Synchrotron Radiation Center, Hiroshima University, Higashi-Hiroshima, 739-0046, Japan*
[d] *Institute for Materials Research, Tohoku University, Sendai 980-8577, Japan*

Keywords: Metallic glasses, Thermal rejuvenation effect, Heterogeneity, Chemical nature.

Recently, Ketov *et al.* [1] proposed a new type of a rejuvenation effect in metallic glasses, *i.e.*, a relaxation to a higher energy state, by a thermal cycle. According to their interpretation, if a glass is not elastically homogeneous, the thermal expansion coefficient has a distribution over the glass sample. By repeated temperature changes, magnitudes of thermal expansions are different depending on the positions in the glass, which surely induces shearing forces, and as a result, a rejuvenation effect occurs in the glass. They named this phenomenon as "Rejuvenation of metallic glasses by non-affine thermal strain". The validity of this logic is now the subject to the discussion.

Yamazaki [2] intensively studied β-relaxation peaks in Gd-TM (TM = Co, Ni, and Cu) glasses. The β-peaks are remarkably larger than those of other metallic glasses, and thus, large heterogeneities are expected in these glasses. He also found that the heterogeneities highly depend on the transition metal elements, *i.e.,* Ni > Co > Cu.

In order to clarify the structural changes by the rejuvenation effect, we measured high-energy x-ray diffraction measurements. The rejuvenation of the glass samples was made by a thermal cycling between the liquid N_2 and room temperatures 40 times. The obtained pair distribution functions, $g(r)$, have two distinct peaks, where the shorter and longer ones (0.29 and 0.35 nm) correspond to the Gd-TM and Gd-Gd correlations, respectively. After the thermal treatments, slight decreases and distance shifts are observed in these peaks. We also performed anomalous x-ray scattering experiments to further investigate partial structures relating to the rejuvenation effect.

In this study, we start to investigate this thermal rejuvenation effect from another point of electronic views. We have recently measured inverse-photoemission spectroscopy (IPES) on these metallic glasses *before the thermal treatments*.

The amorphous samples were prepared by melt spinning with a single Cu roll installed at the Institute for Materials Research, Tohoku University, Sendai, Japan. Ribbon samples with a thickness of about 20 μm and a width of ~ 2 mm were obtained.

The IPES spectra were obtained by using the RIPES spectrometer at HiSOR to measure the conduction-band density of states (DOS). A self-developed IPES spectrometer is equipped with a low-energy electron gun, a non-periodic spherical grating, and a CsI-coated multichannel plate detector [3]. The total energy resolution was ~0.5 eV at the electron gun energy of 50 eV. The energy of the IPES spectra is referred to the Fermi energy determined from an IPES spectrum of a freshly evaporated Au film.

The IPES spectra were collected at room temperature. Clean surfaces were *in situ* obtained by scraping the samples with a diamond filer in a sample preparation chamber attached with the analyzer one, both of which were kept under ultrahigh vacuum below 1×10^{-8} Pa.

Figure 1 shows IPES spectra of well-relaxed (a) $Gd_{65}Co_{35}$ and (b) $Gd_{65}Cu_{35}$ metallic glass alloys. In (a), three structures are observed in this conduction-band DOS, i.e., a shoulder at 2.5 eV, a main peak at 8,5 eV, and a second peak at about 18 eV. By replacing Co with Cu, the magnitude of the shoulder becomes much weaker. The main peak position shifts towards the lower energy by about 1.5 eV, while that of the second peak remain mostly unchanged. The electronic origins of these structures, the element and orbital angular momentum, are now under consideration.

In the next experimental round, we would like to measure PES and IPES spectra of the same glassy samples *after* the thermal cycling by 40 times between liquid N_2 and room temperatures. Since the atomic structures are clearly changed by this rejuvenation effect, the electronic structures should be correspondingly affected. We hope that clear spectral contrasts distinctly appear in the electronic structures by the rejuvenation effect of thermal cycling.

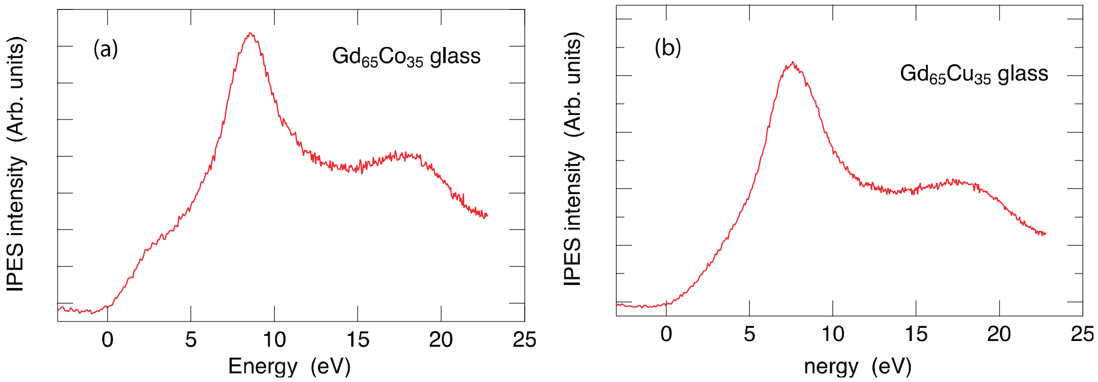

FIGURE 1. IPES spectra of well-relaxed (a) $Gd_{65}Co_{35}$ and (b) $Gd_{65}Cu_{35}$ metallic glass alloys.

This work was performed under the inter-university cooperative research program of the Institute for Materials Research, Tohoku University (Project Nos. 17K0050, 18K0010, 19K0005, and 19K0605). The IPES experiments were performed with the RIPES station in the HiSOR with the approval of the Hiroshima Synchrotron Radiation Center (No. 20AG024).

REFERENCES

1. S. V. Ketov, Y. H. Sun, S. Nachum, Z. Lu, A. Checchi, A. R. Beraldin, H. Y. Bai, W. H. Wang, D. V. Louzguine-Luzgin, M. A. Carpenter, and A. L. Greer, *Nature* **524**, 200-203 (2015).
2. Y. Yamazaki, *Thesis* (Tohoku University, 2016).
3. M. Arita, H. Sato, M. Higashi, K. Yoshikawa, K. Shimada, M. Nakatake, Y. Ueda, H. Namatame, M. Taniguchi, M. Tsubota, F. Iga, and T. Takabatake, *Phys, Rev. B* **75**, 205124 (2007).

Low-Energy Photoemission Study of YbCu$_{5\text{-}x}$Al$_x$

A. Kano [a], R. Kamimori[a], T. Matsumoto[b], H. Sato[c], M. Arita[c], N. Tsujii[d]

[a] *Faculty of Science, Hiroshima University, Higashi-Hiroshima 739-8526, Japan*
[b] *Graduate School of Science, Hiroshima University, Higashi-Hiroshima 739-8526, Japan*
[c] *Hiroshima Synchrotron Radiation Center, Hiroshima University, Higashi-Hiroshima 739-0046, Japan*
[d] *Quantum Beam Unit, National Institute for Materials Science, Tsukuba 305-0047, Japan*

Keywords: Yb-compound, Kondo peak, quantum critical point

YbCu$_{1\text{-}x}$Al$_x$ runs from the non-magnetic to magnetic regions in the Doniach phase diagram with the Al concentration (x), across the quantum critical point (QCP) around x = 1.5 [1]. YbCu$_5$, actual composition of YbCu$_{6.5}$, is located in the he non-magnetic Fermi liquid phase and the Kondo temperature $T_{\rm K}$ is estimated to be around 1000 K (see Fig. 1 (b)). With increasing x, $T_{\rm K}$ is decreased and an antiferromagnetic order appears below 1 K for $x \geq 1.5$. In case of Yb compounds, so called the Kondo peak is observed in the low-energy photoemission spectra (LEPES spectra) as a peak near the Fermi level ($E_{\rm F}$) at $k_{\rm B}T_{\rm K}$ [2]. In this study, we measured the LEPES spectra of YbCu$_{1\text{-}x}$Al$_x$ ($0 \leq x \leq 2$) at undulator beamline BL-9A. Clean surfaces of the polycrystalline samples were prepared by fracturing *in situ*.

Figure 1 (a) shows the x-dependence of the LEPES spectra of YbCu$_{1\text{-}x}$Al$_x$ measured at $h\nu$ = 14 eV and T = 15 K. The characteristic peaks near $E_{\rm F}$ are attributed to the Kondo peak. With increasing x, the peak is shifted to $E_{\rm F}$ and intensity becomes weak, which reflects the decrease of $T_{\rm K}$. The energy positions of the Kondo peak are plotted as a function of x in Fig. 1 (b). The peak energies rapidly decrease for $0 \leq x \leq 0.8$ and slowly decreases above x = 0.8. The $T_{\rm K}$-values are also plotted in the figure [3]. Appropriate vertical offset and scale change are made for comparison. It is noticed that their x-dependences are similar, although peak energies do not correspond to $k_{\rm B}T_{\rm K}$. The Kondo peak is weakly observed still for $x \geq 1.5$, suggesting a presence of the hybridization between the Yb 4*f* electrons and conduction electrons in the magnetic region across QCP.

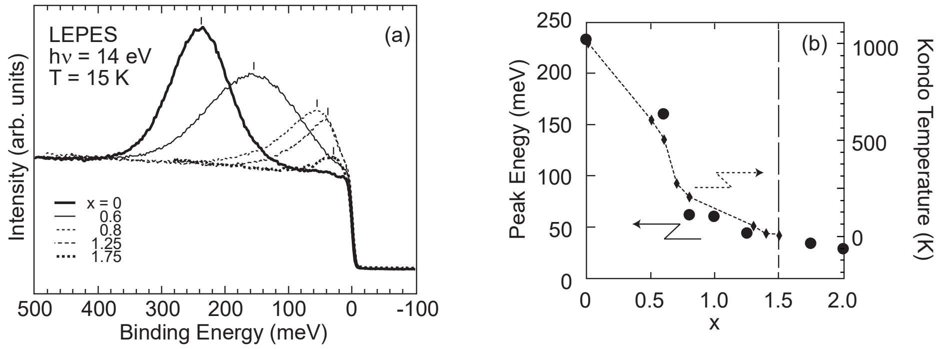

FIGURE 1. (a) LEPES spectra of YbCu$_{1\text{-}x}$Al$_x$ measured at hν=14 eV and T=15 K. (b) Al-concentration(x)-dependences of energy position of the Kondo peak (circles) and Kondo temperature (diamonds).

REFERENCES

1. E. Bauer *et al.*, Phys. Rev. B **56**, 711 (1997).
2. K. Yoshikawa *et al.*, Phys. Rev. B **72**, 165106 (2005).
3. H. Yamaoka *et al.*, Phys. Rev. B **80**, 035120 (2009).

Electronic structure of $NaSn_2As_2$ studied by angle-resolved photoemission spectroscopy

T. Mizokawa[a], Y. Akabane[a], T. Shimaiwa[a], N. L. Saini[b],
Y. Goto[c], Y. Mizuguchi[c], M. Arita[d]

[a] *Department of Applied Physics, Waseda University, Shinjuku-ku, Tokyo 169-8555, Japan*
[b] *Department of Physics, University of Roma "La Sapienza", Piazzale Aldo Moro 2, 00185 Roma, Italy*
[c] *Department of Physics, Tokyo Metropolitan University, Hachioji 192-0397, Japan*
[d] *HiSOR, Hiroshima University, Higashihiroshima, Hiroshima 739-0046, Japan*

Keywords: Superconductivity, Thermoelectric material, Dirac cone

The layered materials with BiS_2 planes exhibit both high thermoelectric performance and superconductivity [1]. Their Fermi surfaces are mainly constructed from the Bi $6p_x/6p_y$ orbitals which are responsible for the exotic superconductivity and the lattice anomalies [2]. The structural instability induced by the Bi 6*p* orbital degeneracy plays important roles for the suppression of lattice thermal conductivity which is one of the prerequisites for high thermoelectric performance. Very recently, new layered materials with SnAs planes have been found to exhibit superconductivity and relatively high thermoelectric performance [3,4] whose electronic and lattice properties somewhat resemble those of the BiS_2-based materials. The band structure of $NaSn_2As_2$ has been studied by means of angle-resolved photoemission spectroscopy [5]. The overall band structure is roughly reproduced by band-structure calculations [5,6]. However, the electron pocket observed at the Γ point does not agree with the band-structure calculations in which bottom of the electron band is well above the Fermi level [6]. In order to understand reasons of the disagreement between the experiment and the theory, we have performed angle-resolved photoemission spectroscopy of $NaSn_2As_2$.

ARPES measurements were performed at beamlines 9A of HiSOR. The crystal was cleaved at 30 K under the ultrahigh vacuum and measured at 30 K. The excitation energy hν was set to 20 eV. The total energy resolution was about 30 meV. In the band map shown in Fig. 1, which was taken just after the cleaveage, an electron band is observed at the center where k_z (wave number perpendicular to the surface) corresponds to the Z point. In the momentum distribution curves, the bottom of the electron band exhibits a Dirac-like dispersion.

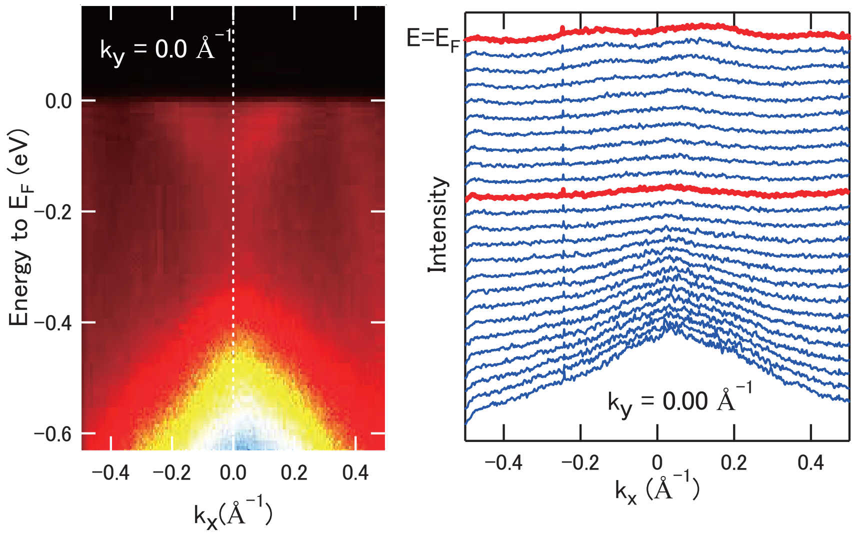

FIGURE 1. Band map and momentum distribution curves taken at hν = 20 eV just after the cleavage.

Figure 2 shows a Femi surface map which was taken a few hours after the cleavage. The electron pocket observed in Fig. 1 disappeared probably due to surface aging. Instead, the flower-shaped Fermi surface from the bulk is clearly observed. As reported in ref. 7, the entire valence band did not shift by the aging, excluding energy shift by removal of electrons from the surface [7]. Therefore, the electron pocket in Fig. 1 can be assigned to a surface state rather than the bulk conduction band whose bottom is located at the Z point. The Dirac-like dispersion shown in Fig. 1 may indicate some topological nature of the title system.

The geometry of the bulk Fermi surface is roughly consistent with the band structure calculations [6] while the band dispersions are modified from the calculations probably due to electronic correlation effects [7]. The Fermi surface is electron-like around the M point while it is hole like around the Γ point. The three-dimensional geometry of the Fermi surface should be studied in future in order to understand the axis-dependent sign change of Seebeck coefficient [8].

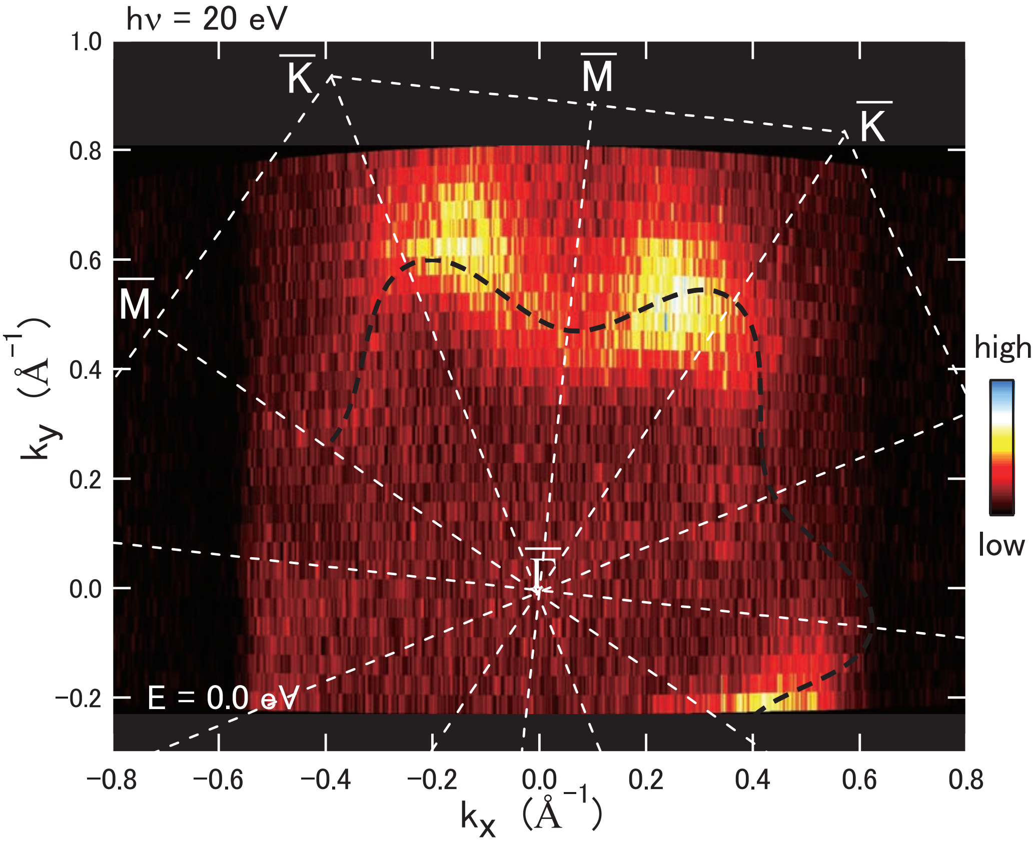

FIGURE 2. Fermi surface map taken at hν = 20 eV a few hours after the cleavage

REFERENCES

1. Y. Mizuguchi, *J. Phys. Soc. Jpn*. **88**, 041001 (2019).
2. K. Terashima, T. Wakita, and T. Yokoya, *J. Phys. Soc. Jpn*. **88**, 041006 (2019).
3. Y. Goto, A. Yamada, T. D.Matsuda, Y. Aoki, and Y. Mizuguchi, *J. Phys. Soc. Jpn*. **86**, 123701 (2017).
4. Y. Goto, A. Miura, C. Moriyoshi, Y. Kuroiwa, T.D. Matsuda, Y. Aoki and Y. Mizuguchi, *Sci. Rep*. **8**, 12852 (2018)..
5. M. Q. Arguilla, J. Katoch, K. Krymowski, N. D. Cultrara, J. Xu, X. Xi, A. Hanks, S. Jiang, R. D. Ross, R. J. Koch, S. Ulstrup, A. Bostwick, C. Jozwiak, D. W. McComb, E. Rotenberg, J. Shan, W. Windl, R. K. Kawakami, and J. E. Goldberger, *ACS Nano* **10**, 9500 (2016).
6. K. Ishihara, T. Takenaka, Y. Miao, O. Tanaka, Y. Mizukami, H. Usui, K. Kuroki, M. Konczykowski, Y. Goto, Y. Mizuguchi, and T. Shibauchi, *Phys. Rev. B* **98**, 020503(R) (2018).
7. Y. Akabane, T. Shimaiwa, Y. Goto, Y. Mizuguchi, T. Yokoya, M. Arita, S. Kumar, E. F. Schwier, K. Shimada, N. L. Saini, T. Mizokawa, *J. Phys. Soc. Jpn*. **89**, 114707 (2020).
8. B. He, Y. Wang, M. Q. Arguilla, N. D. Cultrara, M. R. Scudder, J. E. Goldberger, W. Windl, and J. P. Heremans, *Nat. Mater.* **18**, 568 (2019).

Disentangling spin and orbital texture of surface states of HfSiS

X. X. Wang[a], J. H. Chen[a], M. T. Zheng[a], M. Novak[b], F. Orbanić[b], K. Sumida[a], T. Yoshikawa[a], M. Nurmamat[a], K. Miyamoto, T. Okuda[c], and A. Kimura[a]

[a]*Graduate School of Science, Hiroshima University, 1-3-1 Kagamiyama, Higashi-Hiroshima 739-8526, Japan*
[b]*Department of Physics, Faculty of Science, University of Zagreb, Bijenička 32, 10000 Zagreb, Croatia*
[c]*Hiroshima Synchrotron Radiation Center, Hiroshima University, 2-313 Kagamiyama, Higashi-Hiroshima 739-0046, Japan*

Keywords: non-symmorphic semimetals, spin-orbit coupling, Rashba-type spin-split surface state.

HfSiS is the most representative compound because of the emergence of spin-split surface states (SSs) due to strong spin-orbit coupling at the $\bar{X}$ point with C_{2v} symmetry near the Fermi level [1, 2]. Thus, HfSiS could be a good candidate to realize exotic orbital and spin texture due to spin orbital fields on the surfaces. However, until now, there has been no systematic investigations on the orbital configuration and spin texture of these surface states.

The measurement was performed at $h\nu = 24$ eV using the high-resolution SARPES apparatus (Efficient Spin-resolved Spectroscopy Observation machine: ESPRESSO) installed at beamline BL 9B of the HSRC. The high efficiency of the very low energy electron diffraction (VLEED) spin polarimeters let us perform the SARPES measurements with high energy and angular resolutions ($E \sim$ 20 meV, $\theta \sim \pm 0.35°$). The in-plane (Sx, Sy) and out-of-plane (Sz) spin components of the sample can be obtained by the spin-detector system. The effective Sherman function of the detector was 0.22.

After identifying the orbital character of the surface-derived electron pocket at BL-1 (see Activity Report for 17AG055), we also performed the SARPES and found that SS1 state has intriguing orbital resolved spin texture. To analyze the spin polarization of the SS1 by SARPES, we plotted the spin-up ($I_\uparrow$) and spin-down ($I_\downarrow$) energy-distribution curves (EDCs) and the related spin polarization measured at the different positions of the electron pockets around the $\bar{X}$ points in Figs. 1 (b) and (c). Here we examine spin-resolved EDCs along the $\bar{M}\bar{X}$- line (*i.e.* k_y direction) with k_y position -0.04 Å^{-1} (labeled as 1) and +0.04 Å^{-1} (labeled as 2) in Fig. 1(a). In Figs. 1(b) (i and ii), the EDCs with in-plane spin components (x) exhibit reversed spin polarizations with the opposite k_y momenta with respect to the $\bar{X}$ point, giving clear evidence of a Rashba-type contribution in the spin splitting of the SS1. As expected from symmetry-reflection arguments, in Figs. 1(b) (iii and iv), the spin polarization is negligible for the y component for cuts 1 and 2 (Figs. 1(a) and (d)).

To scrutinize the spin character of this surface-derived electron pocket (SS1), we have also measured SARPES for the upper and lower electron pockets around the $\bar{X}$ point at the positions marked 3-9 in Fig. 1 (d). The measured spin-resolved EDCs for the y spin component for cut 3 (4) (Fig. 1 (b)(v)) and cut 6 (Fig. 1 (b)(vi)) on the inner and outer branch of the upper electron pocket show reversed spin direction. Interestingly, the *x* spin component for cuts 3-6 were found to be negligible (Fig. 1(b) (vii and viii)), which supports a unidirectional spin texture with non-tangential spin orientation being distinct from the conventional Rashba-type spin texture. Noticeably, label 5 on Fig. 1(d) is the ***k*** point on the outer branch close to the corner of the electron pocket, which shows the largest spin polarization for cuts labels 1-6 (see in Fig. 1(b)(v) and Fig. 1(c)(iii-vi)). Furthermore, the spin-resolved EDCs for the y spin component for the cuts labels 7-9 shows the same spin direction (Fig. 1(c)(i)) as in those of the cuts 5 and 6, while negligible *x* spin component was further confirmed as shown in Fig. 1(c)(ii). Thus, we verify an exotic unidirectional spin texture and clarify the whole spin texture of the four electron pockets as shown in Fig. 1(d), where the spin orientation rotates clockwise remaining independent of the momentum as one travels along the inner branch while counter-clockwise for the outer branch for all the electron pockets around the $\bar{X}$ point [3].

REFERENCES

[1] D. Takane, Z. W. Wang, S. Souma, K. Nakayama, C. X. Trang, T. Sato, T. Takahashi, and Y. Ando, Phys. Rev. B **94**, 121108(R) (2016).

[2] R. Lou, J.Z. Ma, Q.N. Xu, B.B. Fu, L.Y. Kong, Y.G. Shi, P. Richard, H.M. Weng, Z. Fang, S.S. Sun, Q. Wang, H.C. Lei, T. Qian, H. Ding, and S.C. Wang, Phys. Rev. B **93**, 241104(R) (2016).

[3] X. X. Wang, J. H. Chen, M. T. Zheng, T. V. Menshchikova, I. P. Rusinov, E. F. Schwier, F. Orbanić, S. L. Wu, K. Sumida, T. Yoshikawa, K. Miyamoto, M. Nurmamat, T. Okuda, K. Shimada, M. Novak, E. V. Chulkov and A. Kimura, Phys. Rev. B **100**, 205140 (2019).

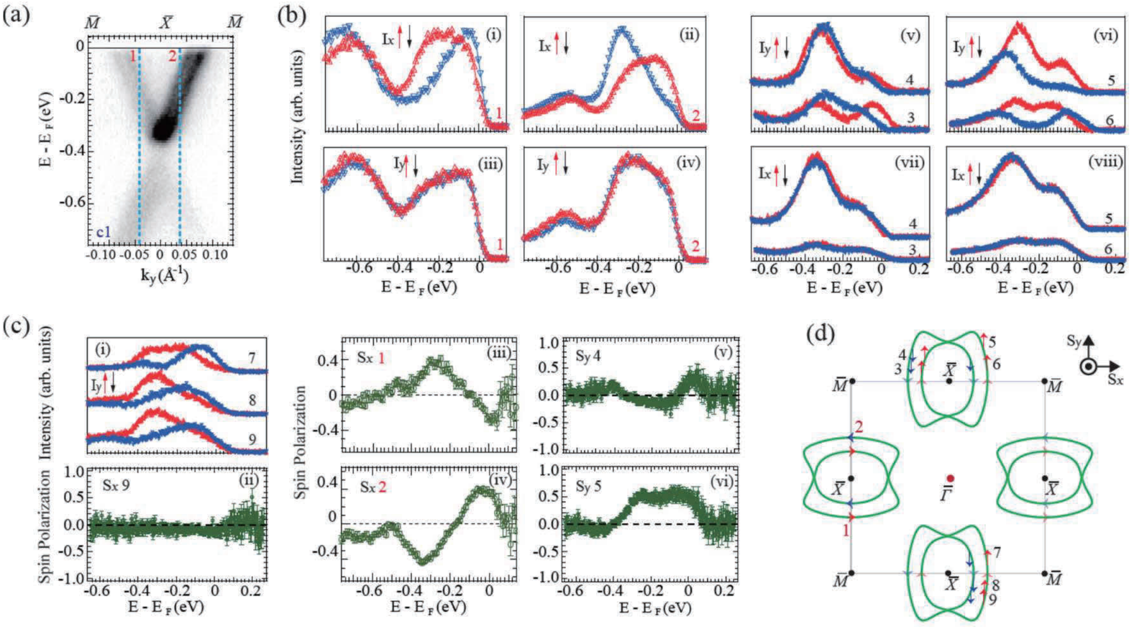

FIG. 1 (a) ARPES dispersion intensity maps of HfSiS with *p*-polarized light acquired with a photon energy ($h\nu$) of 24 eV along the $\bar{M}\bar{X}$-line. (b) SARPES energy distribution curves (EDCs) (red and blue lines show the spin-up and spin-down EDCs), and the wave vector positions of the spin-resolved EDCs [Fig. 1(a) and 1(d)]. (c) (i) Spin-resolved EDCs for the spin components along the *y*-direction measured at the positions marked 7-9 in Fig. 1 (d) and below is the corresponding net *x* component of spin polarization for cut 9. Right is the net *x* component of spin polarization for cut1 (2) and *y* component for cut 4 (5). (d) Schematic figure of the spin texture of the surface-derived electron pocket based on the experimental results.

Variable surface state splitting of DNL semimetal *M*SiS (*X*=Zr, Hf) by tuning SOC coupling strength

X. X. Wang[a], J. H. Chen[a], M. T. Zheng[a], M. Novak[b], F. Orbanić[b], K. Sumida[a], T. Yoshikawa[a], M. Nurmamat[a], K. Miyamoto[c], T. Okuda[c], and A. Kimura[a]

[a]*Graduate School of Science, Hiroshima University, 1-3-1 Kagamiyama, Higashi-Hiroshima 739-8526, Japan*
[b]*Department of Physics, Faculty of Science, University of Zagreb, Bijenička 32, 10000 Zagreb, Croatia*
[c]*Hiroshima Synchrotron Radiation Center, Hiroshima University, 2-313 Kagamiyama, Higashi-Hiroshima 739-0046, Japan*

Keywords: non-symmorphic semimetals, spin-orbit coupling, Rashba-type spin-split surface state.

A spin-split feature of the surface state in HfSiS due to the strong SOC was clearly demonstrated by our spin-resolved ARPES (SARPES) study [1] (also see Activity Report for 17AG057). It is, however, uncertain whether the surface state is spin-split on the ZrSiS (001) plane through the previous angle-resolved photoemission spectroscopy (ARPES). Motivated by this, we have tried to identify the spin-split surface states in both HfSiS and ZrSiS due to the spin-orbit coupling by performing spin- and angle- resolved photoelectron spectroscopy (SARPES).

The measurement was performed at $h\nu$= 24 eV using the high-resolution SARPES apparatus (Efficient Spin-resolved Spectroscopy Observation machine: ESPRESSO) installed at beamline BL 9B of the HSRC. The high efficiency of the very low energy electron diffraction (VLEED) spin polarimeters let us perform the SARPES measurements with high energy and angular resolutions ($E \sim$ 20 meV, $\theta \sim \pm 0.35°$). The in-plane (*Sx*, *Sy*) and out-of-plane (*Sz*) spin components of the sample can be obtained by the spin-detector system. The effective Sherman function of the detector was 0.22.

The ARPES energy band dispersions of ZrSiS along the $\bar{M}\bar{X}$-line [Fig. 1(b)] exhibits a much smaller splitting in comparison with that of HfSiS [Fig. 1(a)]. This certainly stems from the lighter atomic mass and thus weaker SOC of Zr compared to that of Hf. The split-band dispersion is hardly visible in the ARPES spectrum, which has motivated us to make a direct detection of spin polarization of the surface states in ZrSiS. We first plot the spin-up ($I_\uparrow$) and spin-down ($I_\downarrow$) energy distribution curves (EDCs) of HfSiS acquired with *p*-polarized light along the $\bar{M}\bar{X}\bar{M}$ line as well as the corresponding spin-polarization in Fig. 1(b). As expected for the Rashba-type spin-splitting, the spin component along *y*-axis exhibits a difference between spin-up and spin-down intensities. An energy difference between the spin-up and spin-down intensity maxima for the cut *c1* exhibit a magnitude of 190 meV and the absolute spin polarization is ~0.8. The spin-down intensity is dominant near the Fermi level for cut *c1*, suggesting a spin texture of the inner contour of the electronic pocket with a clockwise rotation, while anti-clockwise rotation for the outer contour. The spin-resolved intensities and the spin polarizations of ZrSiS measured along two cuts (*c2* and *c3*) are shown in Fig. 1(d). It certainly proves the presence of Rashba-type spin-splitting with a size of 40 meV and the reversed spin polarizations on the opposite wavenumbers in the surface band dispersion of ZrSiS. A finite spin polarization around 0.25 is observed, which is much smaller than that in HfSiS.

REFERENCES

[1] X. X. Wang, J. H. Chen, M. T. Zheng, T. V. Menshchikova, I. P. Rusinov, E. F. Schwier, F. Orbanić, S. L. Wu, K. Sumida, T. Yoshikawa, K. Miyamoto, M. Nurmamat, T. Okuda, K. Shimada, M. Novak, E. V. Chulkov and A. Kimura, Phys. Rev. B **100**, 205140 (2019).

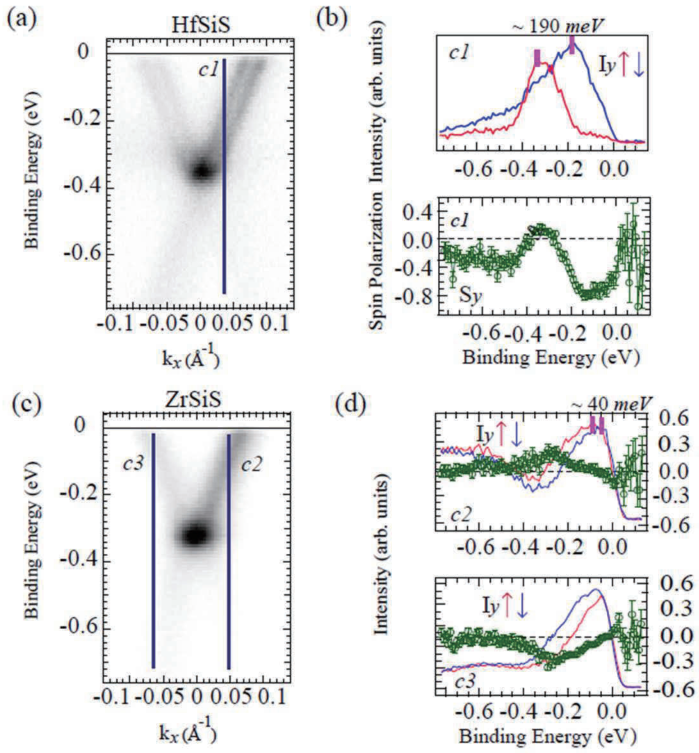

FIG. 1 (a) and (c) ARPES dispersion intensity maps for HfSiS and ZrSiS, respectively. Spin-resolved ARPES momentum distribution curves (EDCs) of HfSiS (b) and ZrSiS (d) (red and blue line show the spin up and spin down EDCs), the wave vector positions of the spin EDCs shown as blue lines mark in panels (a) and (c). The corresponding net *y* component of spin polarization (green circle) is shown.

In-situ evaluation of spin polarizations and band dispersions of Co_2MnSi thin film

Masaaki Kakoki[a], Kazuki Sumida[a], Takashi Kono[a], Kazuki Goto[b],
Koji Miyamoto[c], Taichi Okuda[c], Yuya Sakuraba[b], Kazuhiro Hono[b],
and Akio Kimura[a]

[a]*Graduate School of Science, Hiroshima University, 1-3-1 Kagamiyama, Higashi-Hiroshima 739-8526, Japan*
[b]*National Institute for Materials Science, 1-2-1 Sengen, Tsukuba 305-0047, Japan*
[c]*Hiroshima Synchrotron Radiation Center, Hiroshima University, 2-313 Kagamiyama, Higashi-Hiroshima 739-0046, Japan*

Keywords: vacuum suitcase, half-metallicity, tunneling magnetoresistance ratio, spin polarizations

Many Co-based Heusler alloys are theoretically predicted to be half-metallic ferromagnets, in which the electrons at the Fermi level are 100% spin-polarized, and are promising for spintronic applications such as magnetoresistive random access memory (MRAM) and high-sensitivity magnetic sensors etc.. Among the Co-based Heusler alloys, Co_2MnSi is predicted to exhibit half-metallicity [1], and the tunnel magnetoresistance (TMR) ratio of magnetic tunnel junction (MTJ) based on Co_2MnSi has been measured extensively [2,3]. While the MTJ using Co_2MnSi shows a high TMR ratio at low temperatures, the TMR ratio drops rapidly at room temperature. The reason for this is thought to be the decrease in the spin polarization due to the interface state in the MTJ [4]. To solve this problem, it is necessary to separate the bands related to conduction and observe the correct spin-polarized electronic state. To solve this problem, it is necessary to perform *in-situ* spin- and angle-resolved photoemission spectroscopy (SARPES) measurements on single crystalline thin-film samples. However, no such studies have been performed so far.

In this study, we performed SARPES measurements on Mn-rich Co_2MnSi thin film to clarify the bulk spin-polarized electronic states without the effect of interface states. We fabricated and installed a mechanism for magnetization in an ultrahigh vacuum (UHV) chamber [Fig. 1**a**] at BL-9B, HiSOR, and prepared the apparatus for *in-situ* measurement of thin-film samples transported from the vacuum suitcase chamber. These efforts made it possible to perform SARPES measurements with keeping the sample in the UHV throughout the entire process from the preparation of high-quality single crystalline samples at National Institute for Materials Science (Tsukuba) to the SARPES apparatus at HiSOR (Higashi-hiroshima). As a result, we succeeded in observing a parabolic band crossing the Fermi level, as shown in Fig. 1**b**. Furthermore, the SARPES measurement along the cut line in Fig. 1**b** revealed that the band crossing the Fermi level is positively spin-polarized, indicating that it is a majority-spin band [Fig. 1**d**]. Thus, the half-metallic electronic state of Co_2MnSi has been experimentally verified for the first time.

Our finding is expected to lead to a breakthrough in the application of spintronic devices using Co-based Heusler alloys. In addition, the spin-dependent electronic states of Co-based Heusler alloys play a key role in the mechanism of their unique thermoelectric and magnetic shape memory properties, and SARPES measurements are essential to elucidate these properties.

REFERENCES

[1] S. Ishida *et al*., J. Phys. Soc. Jpn. **64**, 2152 (1995).
[2] Y. Sakuraba *et al*., Appl. Phys. Lett. **88**, 192508 (2006).
[3] B. Hu *et al*., Phys. Rev. B **94**, 094428 (2016).
[4] P. Mavropoulos *et al*., Phys. Rev. B **72**, 174428 (2005).

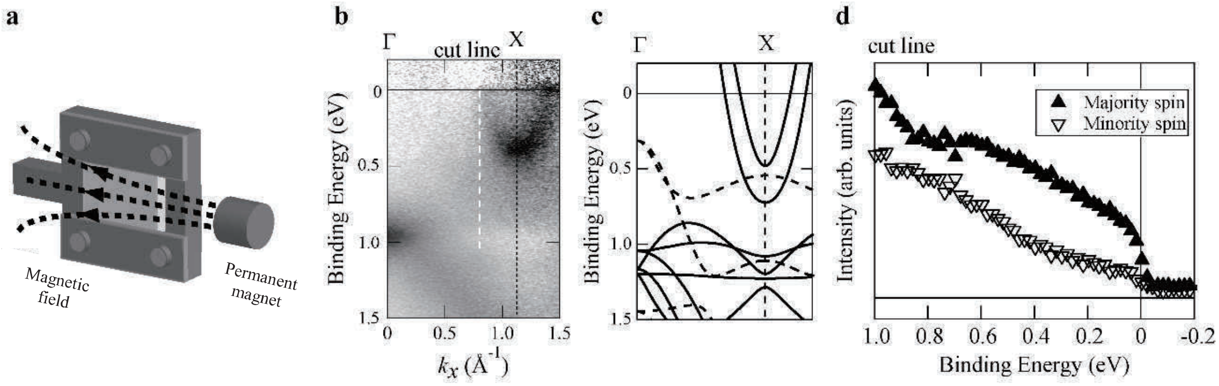

FIG. 1 a Schematic of magnetization before SARPES measurement. **b** Band dispersion of Mn-rich Co$_2$MnSi thin film obtained by ARPES. **c** First-principles calculation results for Co$_2$MnSi. **d** SARPES spectrum of Mn-rich Co$_2$MnSi.

Observation of Rashba splitting in high-T_c cuprate superconductor $YBa_2Cu_3O_7$

H. Iwasawa[a,b], T. Miyashita[c], T. Yoshikawa[c], A. Kimura[c],

K. Miyamoto[b], T. Okuda[b]

[a]*National Institutes for Quantum and Radiological Science and Technology, Japan*
[d]*Hiroshima Synchrotron Radiation Center, Hiroshima University, Japan*
[c]*Graduate School of Science, Hiroshima University, Japan*

Keywords: Spin-resolved ARPES, Cuprate

Strong electron correlations, rather than spin-orbit interaction (SOI), have long been considered to be the most crucial effect for understanding the physics of cuprate superconductors. However, a recent spin-resolved photoemission study showed spin-polarized states that might be caused by SOI in the cuprate superconductor Bi2212 [1]. According to that work, the Fermi surface of Bi2212 displays states in which the spin direction is locked to the electron momentum (*i.e.,* tangential to the Fermi arc), and the highest spin-polarization is at the Fermi nodal line. They also claimed that the helical spin texture, which is similar to the one caused by the Rashba effect, might be caused by the electric field between the CuO_2 bilayer, based on the spin-resolved ARPES results at several momenta. However, unlike a standard Rashba system, the electronic structure of Bi2212 does not show a pair of bands having opposite helical spin textures. Thus, the origin of such spin-polarization in Bi2212 is a hot open question. Suppose the observed spin-polarized states are intrinsic, it is very important to investigate the origin of such spin polarization in the cuprate superconductors. Further insights on this issue might be related to the cuprate superconductivity since the SOI has been neglected in most models (such as the Hubbard model).

Hence, we have performed high-resolution spin-resolved ARPES measurements on another bilayer cuprate system, $YBa_2Cu_3O_{7-\delta}$ (YBCO), at the BL-9B of Hiroshima Synchrotron Radiation Center. High-quality single crystals of optimally-doped YBCO were prepared by (T_c = 93 K) were grown by the crystal pulling technique and detwinned by annealing under uniaxial pressure [2]. The clean and flat surface of the sample was obtained by cleaving *in situ* in an ultrahigh vacuum better than 1×10^{-10} Torr at around 30 K.

The Fermi surface of YBCO is composed of bonding and antibonding bands (BB and AB) of CuO_2 planes and a CuO-chain (CH) band, as schematically drawn in Fig. 1(a). On the other hand, as shown in Fig. 1(b), the ARPES Fermi surface measured with the photon energy of 55 eV with the linear vertical polarization is dominated by the CuO_2 plane bands, and the signals from the CH band is quite weak. Along near the nodal direction [red line in Fig. 1(a)], the bilayer splitting becomes small, but the two BB and AB states can be recognized in the ARPES image [Fig. 1(c)], and they can be more clearly seen in the MDCs at the Fermi level [Fig. 1(d)] and $E = -0.058$ eV [Fig. 1(e)] at which the spin-resolved ARPES data were corrected. As also seen in Figs. 1(d) and 1(e), the experimental MDCs (open circle) can be fit by four Lorentzian peaks assuming two sets of BB and AB with the linear background.

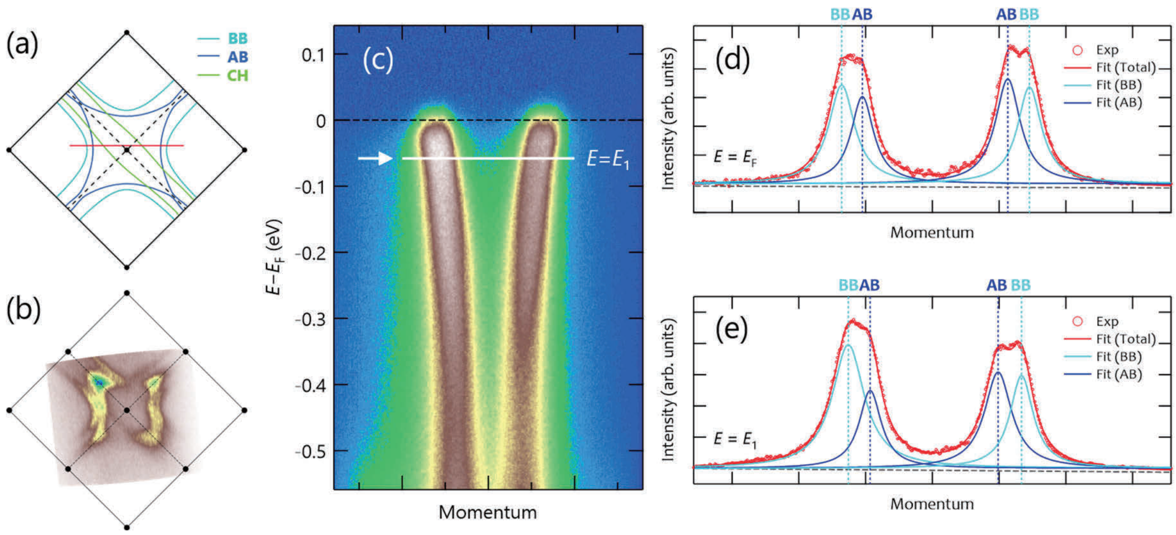

FIGURE 1. (a) and (b) Schematic and ARPES-measured Fermi surface of YBCO. The Fermi surface is composed of the bonding band (BB) and antibonding band (AB) of CuO_2 planes, and CuO chain band (CH). (c) ARPES image taken at the photon energy of 50 eV with linear vertical polarization along near the nodal line, as indicated by the red line in (a). The white line indicates the energy (E_1=–0.058 eV) at which the spin-resolved ARPES data were corrected. Note that the constant background was subtracted from the image. (d) and (e) Spin-integrated MDC at the Fermi level and $E=E_1$, respectively, where the experimental curves (open circles) were fitted by the four Lorentzian peaks with a linear background.

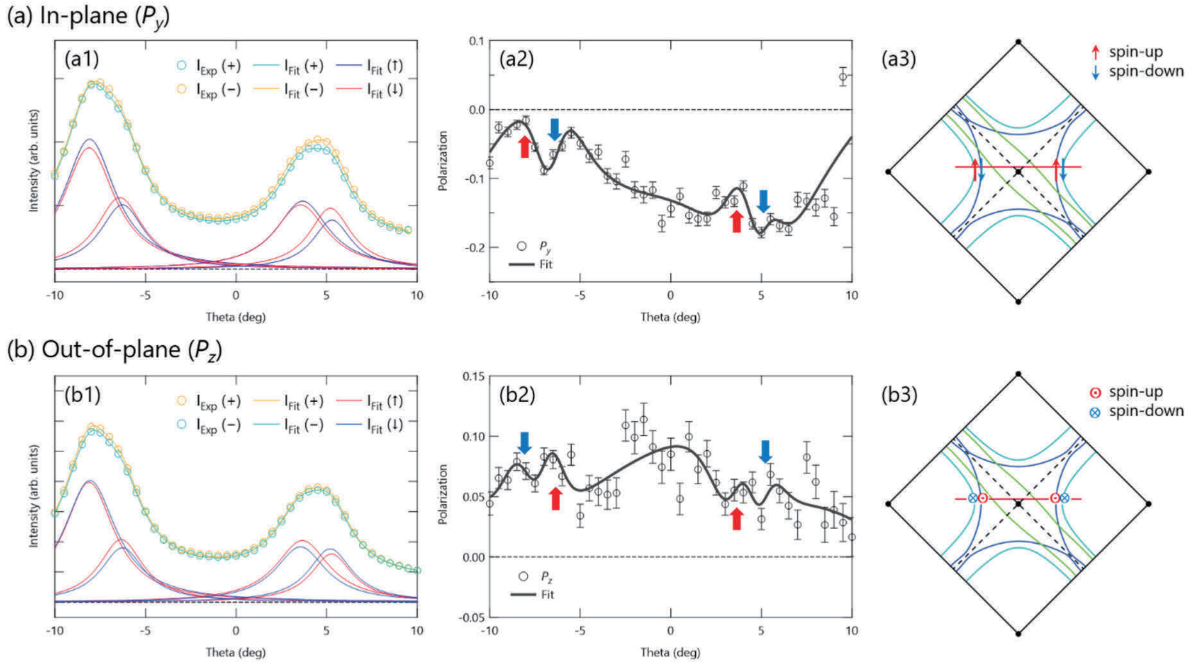

FIGURE 2. (a) and (b) Spin-resolved MDC of YBCO for the in-plane and out-of-plane spin polarization, respectively, taken at E_1=–0.058 eV along near the nodal line at a photon energy of 55 eV with the linear vertical polarization. (a1), (b1) Reflected MDC intensities, I_{EXP} (+) and I_{EXP} (–), taken with the positive and negative magnetized ferromagnetic target, respectively. Spin-resolved MDCs of two-sets of BB and AB, I_{Fit} (↑) and I_{Fit} (↓), were derived from the fits of the reflected MDC intensities [I_{Fit} (+) and I_{Fit} (–)]. (a2) and (b2) The calculated spin polarization, P_y and P_z, respectively. The red and blue arrows represent the spin-up and spin-down polarization, respectively, marked at the peak positions of each band. (a3) and (b3) Measured spin polarization direction for the in-plane and out-of-plane components, respectively.

Figures 2 (a) and (b) show the spin-resolved ARPES results on YBCO for the in-plane and out-of-plane spin polarization (P_y and P_z), respectively. The spin MDC measurements were performed at E=-0.058 eV along near the nodal line using the photon energy of 55 eV and the linear vertical polarization. The reflected MDC intensities, I_{EXP} (+) and I_{EXP} (-), were corrected with the positive and negative magnetization, respectively. The spin polarization can then be calculated as shown in Figs. 2(a2) and (b2). Although the obtained polarization shows non-zero values, it is not straightforward to estimate the spin-polarization direction and magnitude for each BB and AB state. We thus performed the lineshape analysis and found the fitting using four Lorentzian peaks with the linear background can reproduce the experimental curves very well, as seen in Figs. 2(a1) and (b1). Accordingly, the spin-polarization for each BB and AB state can be easily seen from the spin-MDCs [I_{Fit} (↑) and I_{Fit} (↓)] obtained from the fitted intensities, I_{Fit} (+) and I_{Fit} (-). The observed in-plane and out-of-plane spin-polarization are overlaid on the spin polarization in Figs. 2(a2) and (b2) and the schematic Fermi surface in Figs. 2(a3) and (b3). As seen in Fig. 2(a3), the BB and AB state shows the opposite direction for the in-plane spin polarization. Since they are reversed with respect to the Γ point, the in-plane spin texture seems to be helical, consistent with the previous work [1]. As for the out-of-plane spin polarization, we see the opposite direction between the BB and AB states, as shown in Fig. 3(b), while they seem to preserve the same polarization direction on each Fermi surface sheet. On the other hand, we also observed the different tendencies for the in-plane and out-of-plane spin polarization when using the different photon energy of 50 eV (not shown): in-plane spin polarization preserves the same polarization direction with respect to the Γ point, and no out-of-plane spin polarization was observed. Thus, further investigations such as *k*-dependent and photon-energy-dependent spin-ARPES measurements are necessary to pin down the origin of the observed spin polarization.

REFERENCES

1. K. Gotlieb *et al.*, Science **362**, 1271-1275 (2018).
2. Y. Yamada and Y. Shiohara, Physica C **217**, 182 (1993).

Spin-resolved ARPES study of Heusler-type Co_2MnGa exhibiting gigantic anomalous Nernst effect

Kazuki Sumida[a], Yuya Sakuraba[b], Keisuke Masuda[b], Takashi Kono[a], Masaaki Kakoki[a], Kazuki Goto[b], Koji Miyamoto[c], Yoshio Miura[b], Taichi Okuda[c], and Akio Kimura[a]

[a]*Graduate School of Science, Hiroshima University, 1-3-1 Kagamiyama, Higashi-Hiroshima 739-8526, Japan*
[b]*National Institute for Materials Science, 1-2-1 Sengen, Tsukuba 305-0047, Japan*
[c]*Hiroshima Synchrotron Radiation Center, Hiroshima University, 2-313 Kagamiyama, Higashi-Hiroshima 739-0046, Japan*

Keywords: thin films, vacuum suitcase, anomalous Nernst effect (ANE), Weyl cone

The anomalous Nernst effect (ANE) is a phenomenon in which an electric field is generated in the direction perpendicular to the temperature gradient and the magnetization. The thermoelectric potential due to the ANE has been thought to be proportional to the magnitude of magnetization, but recently it has become clear that this rule of thumb breaks down in several magnetic materials, including antiferromagnets [1]. In particular, the thermoelectric potential at room temperature in the ferromagnetic Heusler alloy Co_2MnGa reaches about 6.0 μV/K, which is comparable to about ten times the size of typical ferromagnetic materials such as Fe [2]. The topologically nontrivial electronic structure near the Fermi level (E_F) is thought to play an important role in the giant ANE. However, the exact relationship between the ANE and the electronic structure has not yet been clarified.

To explore the electronic band structures of Co_2MnGa thin films, we performed a spin- and angle-resolved photoelectron spectroscopy (SARPES) experiments for Co_2MnGa with a valence electron number of 27.3 at the ESPRESSO end-station (BL-9B) of HiSOR. For SARPES measurements, uncapped films were deposited on a MgO substrate with buffer layers at room temperature by the magnetron sputtering method at the National Institute for Materials Science. To avoid surface contaminations, grown films were transferred from the magnetron sputtering chamber to the preparation chamber of the SARPES instrument using a portable suitcase chamber to avoid exposure to air ($<1 \times 10^{-6}$ Pa). During all SARPES measurements, the temperature was maintained below 40 K. Before each measurement, the sample was annealed at 550 °C for 30 min at the preparation chamber (base pressure $\sim 4 \times 10^{-8}$ Pa). The quality and cleanliness of the annealed sample was checked by low-energy electron diffraction. A magnetic field as large as ~0.1 T was applied to the samples along the [110] easy-axis using a permanent magnet in the preparation chamber at room temperature. A 0.1 T magnetic field was sufficiently high to saturate the magnetization. The energy and angular resolutions were set to 55 meV and ±1.5°, respectively. The effective Sherman function was 0.28 for the SARPES measurements.

Figures 1(a) and 1(b) show the observed Fermi surface and wide range ARPES image along Γ–K–X line recorded at 50 eV photon energy with *p*-polarized light. At X point, the electron pocket crossing E_F can be seen while the large hole-pocket is located at Γ point. In Figs. 1(c) and 1(d), we present the magnified ARPES image along the Γ–K–X direction and its second derivative along the momentum axis. Around -0.60 Å^{-1} near E_F, one can see a tilted band, in which the node is slightly located above E_F (see gray arrow in Fig. 1(d)). As we can see in Fig. 1(f), this tilted band has a strong majority-spin component. These experimental results agree with the results of the calculation, shown in Fig. 1(e) with the position of E_F shifted downward by 220 meV. Therefore, we conclude that the tilted cone close to K point corresponds to the Weyl cone, which should be responsible for the giant ANE [4].

REFERENCES

[1] M. Ikhlas *et al.*, Nat. Phys. **13**, 1085 (2017).
[2] A. Sakai *et al.*, Nat. Phys. **14**, 1119 (2018).
[3] K. Sumida, Y. Sakuraba, K. Masuda, T. Kono, M. Kakoki, K. Goto, K. Miyamoto, Y. Miura, T. Okuda, and A. Kimura, Commun. Mater. **1**, 89 (2020).

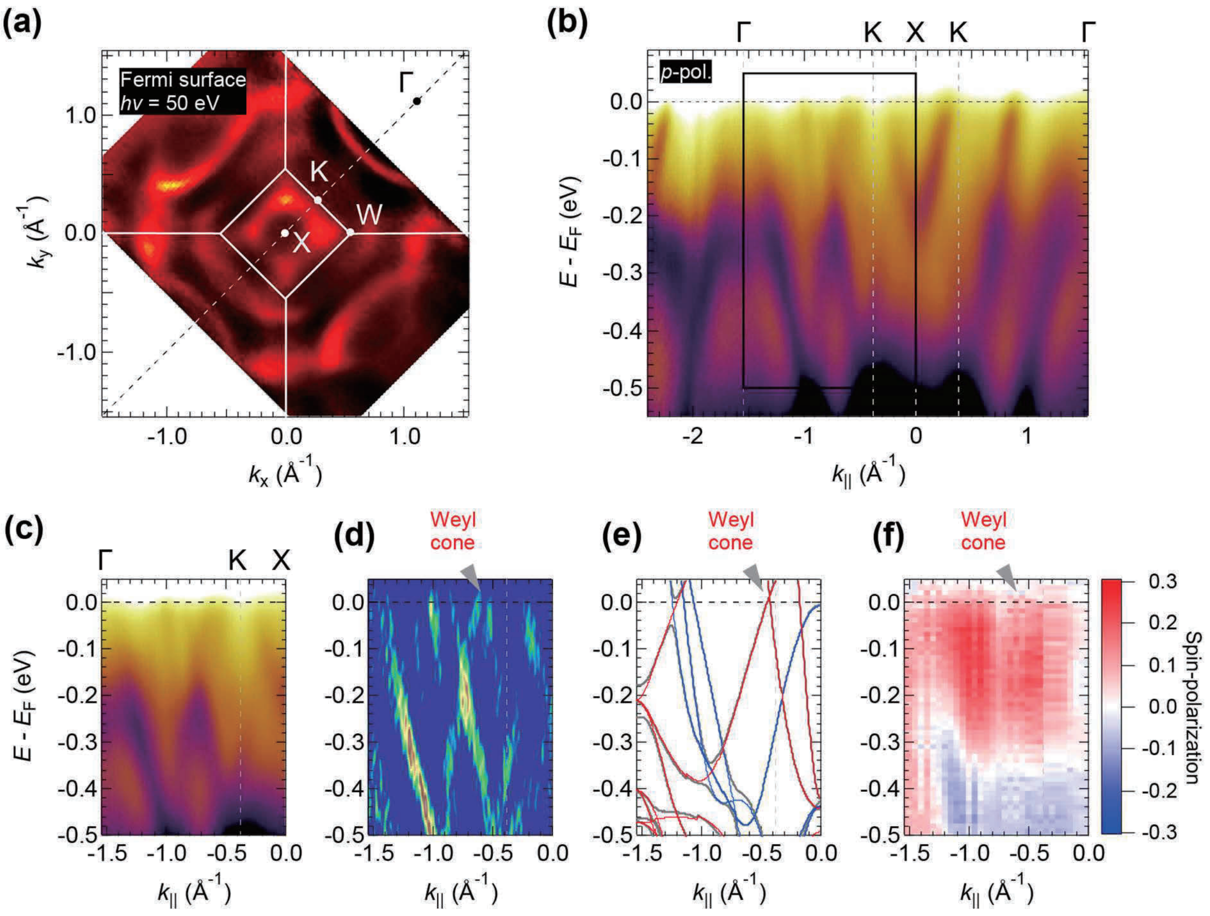

FIG. 1 Observed spin-polarized band structures of a hole-doped Co$_2$MnGa film. (a) Fermi surface of the sample with a valence electron number of 27.3 recorded at 50 eV with *p*-polarized light. (b) Wide ARPES image along the Γ–K–X line indicated by the white dashed line in (a). (c)(d) Magnified ARPES image in the frame in (b) and its second derivative. (e)Calculated band dispersion with E_F shifted downward by 220 meV. (f) Spin-polarization map along the Γ–K–X line.

Spin-polarized tiled Weyl cone in Co_2MnGa thin film probed by spin- and angle- resolved ARPES

Kazuki Sumida[a], Yuya Sakuraba[b], Keisuke Masuda[b], Takashi Kono[a],
Masaaki Kakoki[a], Kazuki Goto[b], Koji Miyamoto[c], Yoshio Miura[b],
Taichi Okuda[c], and Akio Kimura[a]

[a]*Graduate School of Science, Hiroshima University, 1-3-1 Kagamiyama, Higashi-Hiroshima 739-8526, Japan*
[b]*National Institute for Materials Science, 1-2-1 Sengen, Tsukuba 305-0047, Japan*
[c]*Hiroshima Synchrotron Radiation Center, Hiroshima University, 2-313 Kagamiyama, Higashi-Hiroshima 739-0046, Japan*

Keywords: anomalous Nernst effect (ANE), Weyl cone, Berry curvature

Thermoelectric conversion enables us to convert heat into electricity, which is a key technology for a self-sustaining power source in various type of sensors of the Internet of Things (IoT). The thermoelectric conversion technologies have so far been based on the so-called Seebeck effect (SE), which generates an electric field in a direction parallel to the heat flow. It results in the fact that the widely used SE-based device consists of multiple columns of different thermoelectric materials connected in series, leading to a complex structure. The anomalous Nernst effect (ANE), on the other hand, is known to be a phenomenon, in which the propagation direction of carriers is curved by the magnetization of the material, resulting in an electric field in the direction perpendicular to both magnetization and heat flow. It simplifies a device structure and enables thermoelectricity to be generated over a large area. Nevertheless, there has been a hurdle that needs to be overcome, the small thermopowers, for thermoelectric applications. Recently, the room temperature thermoelectric power of the ferromagnetic Heusler alloy Co_2MnGa reaches about 6.0 μV/K, which is about 10 times larger than that of a typical ferromagnetic material such as Fe [1]. The topologically nontrivial electronic structure in the vicinity of the Fermi level plays an important role in such a giant ANE.

To clarify the relationship between thermoelectricity and electronic structure due to ANE, we have performed spin- and angle-resolved photoelectron spectroscopy (SARPES) and first-principles calculations on Co_2MnGa thin films with precisely controlled composition.

The wide range ARPES images were taken along the Γ–K–X line taken at 80 eV energy for incident photons with *p*- and *s*-polarization. With *s*-polarized light, a sharp electron-pocket is markedly enhanced around the X points, whereas the photoemission intensities of the tilted Weyl cone and the flat band observed by *p*-polarization have mostly diminished [2]. In Figs. 1(a) and 1(b), we present the ARPES image and its second derivative with the calculated band structure. Here, to eliminate the effect of the light polarization-dependent matrix element, the images acquired with *p*- and *s*-polarized light are mixed. The experimental result is well reproduced by the calculations with the Fermi level (E_F) shifted upward by 70 meV (i.e., electron doping). This chemical potential shift is consistent with a higher valence electron number (N_v) of 28.5 for this sample than the stoichiometric one ($N_v = 28.0$). Small discrepancies are noted between the observed and calculated band dispersions [Fig. 1(b)], for instance, the location of the bottom of the band of the sharp electron-pocket around the X points. The differences may arise through correlation or k_z broadening effects.

Figure 1(c) shows the magnified ARPES image in the frame shown in Fig. 1(a). With suppression through the matrix-element effect, the band structure around the X point at the $k_z = 2\pi/a$ plane in the second Brillouin zone are clearly visualized. In a comparison with the calculation (Fig. 1(c), lower panel), we realized that the observed band structure around the X point resembles the tilted and gapped Weyl cone. Because the upper part of the Weyl cone cannot be seen, E_F is probably located in the gap of the massive Weyl cone. Here, we turn our attention to the flat band observed around the Γ point. To clarify the origin of the flat band, we show the photon-energy-dependent energy distribution curves (EDCs) at $k_{||} = -0.5$ Å^{-1} taken after magnetization [Fig. 1(d)]. The prominent peaks caused by the flat band do not show a clear photon energy (k_z) dependence. We therefore conclude that the observed flat band just below E_F belongs to a surface state.

REFERENCES

[1] A. Sakai *et al*., Nat. Phys. **14**, 1119 (2018).
[2] K. Sumida, Y. Sakuraba, K. Masuda, T. Kono, M. Kakoki, K. Goto, K. Miyamoto, Y. Miura, T. Okuda, and A. Kimura, Commun. Mater. **1**, 89 (2020).

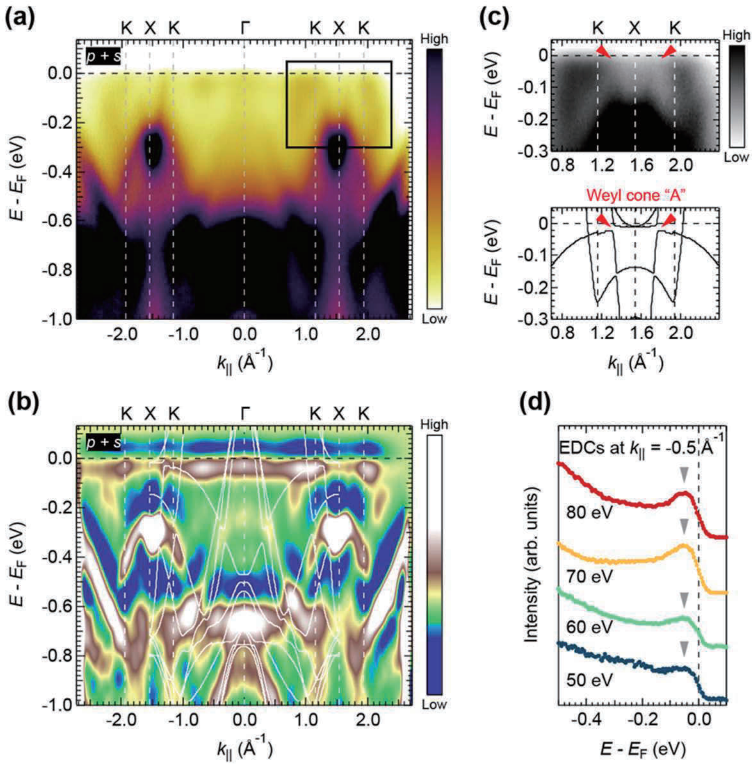

FIG. 1 Observed band structures of an electron-doped Co$_2$MnGa film. (a) ARPES image with *p*-polarized light superimposed with that with *s*-polarized light (b) Second derivative ARPES image of (a) with respect to the energy and momentum directions. The calculated band dispersion is overlaid. (c) Magnified ARPES image (upper) in the frame in (a) and corresponding calculation (lower). (d) Photon-energy-dependent EDCs at $k_{||} = -0.5$ Å^{-1} taken at 50, 60, 70, and 80 eV with *p*-polarized light.

20AG019 BL-9B

Spin-resolved ARPES study of a charge density wave compound $NbTe_4$

M. Sakano[a], N. Mitsuishi[a], M. Chiba[b],
K. Miyamoto[c], T. Okuda[c], T. Sasagawa[b], K. Ishizaka[a]

[a]Quantum-Phase Electronics Center (QPEC) and Department of Applied Physics,
The University of Tokyo, Hongo 113-8656, Japan.
[b]Materials and Structures Laboratory, Tokyo Institute of Technology,
Yokohama 226-8503, Japan.
[c]Hiroshima Synchrotron Radiation Center (HSRC), Hiroshima University,
2-313 Kagamiyama, Higashi-Hiroshima 739-0046, Japan.

Keywords: $NbTe_4$, charge density wave, topological surface states, spin-resolved ARPES

Transition metal tetratelluride MTe_4 (M = Nb, Ta) has a quasi-one-dimensional structure, consisting of linear M chains along c axis and Te squire antiprisms surrounding them [1, 2]. The ground state of MTe_4 is known to a (2×2×3) charge density wave (CDW) state, while their electrical resistivity shows metallic behavior down to the lowest temperature [3]. Recently, magnetoresistance measurement in $TaTe_4$ reports a resistivity plateau and quantum oscillations, suggesting the existence of topological surface states in this system [4]. On the other hand, the seminal angle-resolved photoemission spectroscopy (ARPES) study did not observe clear band dispersion near the Fermi level [5].

In this study, we investigate the electronic band structure and its spin texture of $NbTe_4$ by spin-resolved ARPES at BL-9B (HiSOR). High-quality single crystalline $NbTe_4$ were grown by Te flux method. Samples were cleaved at 230 K in-situ to obtain clean cleavage *ac* planes and cooled down to 20 K. For spin-resolved measurements, we adopted a *s*-polarized 53 eV light and set the energy and angle resolutions to 60 meV and ±1.5 deg, respectively.

Figure 1 (a) shows the spin-integrated ARPES spectra at 20 K along the $\bar{\Gamma}-\bar{Z}$ direction, i.e., parallel to Nb chains (here, $\bar{Z}$ is a high symmetry point of non-CDW phase). Several band dispersions are observed below the binding energy of ~0.4 eV, similarly to the previous ARPES spectra in $TaTe_4$ [5]. Figure 1 (b) shows ARPES spectra near the Fermi level with a different color scale. We find slight but fine band dispersions in this energy region. These bands are more clearly confirmed in the second-momentum-derivative image shown in Fig. 1 (c) (yellow arrows). We focused on these bands and performed spin-resolved measurements (spin component: parallel to *a*-direction). Figure 1 (d) shows the spin-resolved energy distribution curves at two respective momenta (k = -0.19 and 0.28 $Å^{-1}$). This pair of bands has an anti-symmetric spin-up/down contrasts with respect to the $\bar{\Gamma}$ point (see also Fig. 1 (c)), possibly related to the topological states as proposed in the magnetoresistance measurement [4]. For clarifying the origin of these band structures, further theoretical (slab) band calculations and photon-energy-dependent ARPES measurements will be highly desired.

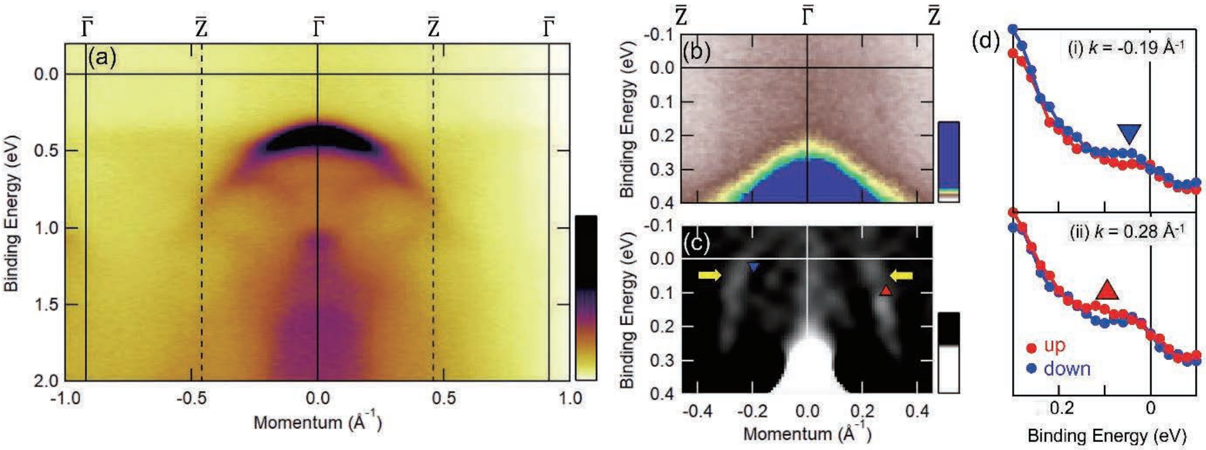

FIGURE 1. (a) Spin-integrated ARPES spectra of $NbTe_4$ along $\bar{\Gamma}-\bar{Z}$ (photon energy: 53 eV, temperature: 20 K). (b) Spin-integrated ARPES spectra near the Fermi level with a different color scale. (c) The second-momentum-derivative image of (b). The yellow arrows indicate band dispersions near the Fermi level. (d) Spin-resolved energy distribution curves at two respective momenta (spin component: parallel to *a*-direction). The red/blue triangular markers indicate slight spin-up/down contrasts.

REFERENCES

1. K. Selte and A. Kjekshus, Acta Chem. Scand. **18,** 690 (1964).
2. E. Bjerkelund and A. Kjekshus, Z. Anorg. Allg. Chem. **328,** 235 (1964).
3. S. Tadaki *et al*., Synth. Met. **38,** 227 (1990).
4. X. Luo *et al*., Appl. Phys. Lett. **110,** 092401 (2017).
5. F. Zwick *et al*., Phys. Rev. B **59,** 7762 (1999).

Probing a New Type of Spin-splitting Effect in Antiferromagnets

Yupeng Zhu[a], Ke Zhang[b], Xiaoming Ma[a], K. Shimada[b], T. Okuda[b], Chang Liu[a]

[a] Shenzhen Institute for Quantum Science and Engineering (SIQSE) and Department of Physics, Southern University of Science and Technology (SUSTech), Shenzhen 518055, China.
[b] Hiroshima Synchrotron Radiation Center, Hiroshima University, Higashi-Hiroshima, Hiroshima 739-0046, Japan

Keywords: spin splitting, spin-resolved, collinear antiferromagnets

Momentum-dependent spin splitting effects are conventionally believed to become distinct only in the materials with structural asymmetry and strong spin-orbit coupling (SOC), including Rashba and Dresselhaus effect [1, 2]. S. Pekar and E. Rashba have predicted that another SOC independent spin-splitting effect exists in inhomogeneous magnets many years ago [3]. Since electron spins are intertwined with their position in the lattice, the spins would flip in response to an external electric field in these systems, leading to a brand-new type of spin splitting that exists without SOC – totally different from the Rashba and Dresselhaus picture [4]. Recently, several works predicted that this effect can exist in antiferromagnets, such as RuO_2, and its energy scale is much larger than most ordinary Rashba and Dresselhaus effects [5, 6]. Up to now, this effect has only been studied theoretically; its experimental discovery is yet to come. We performed the spin and angle-resolved photoemission spectroscopy measurements on RuO_2 at BL09B.

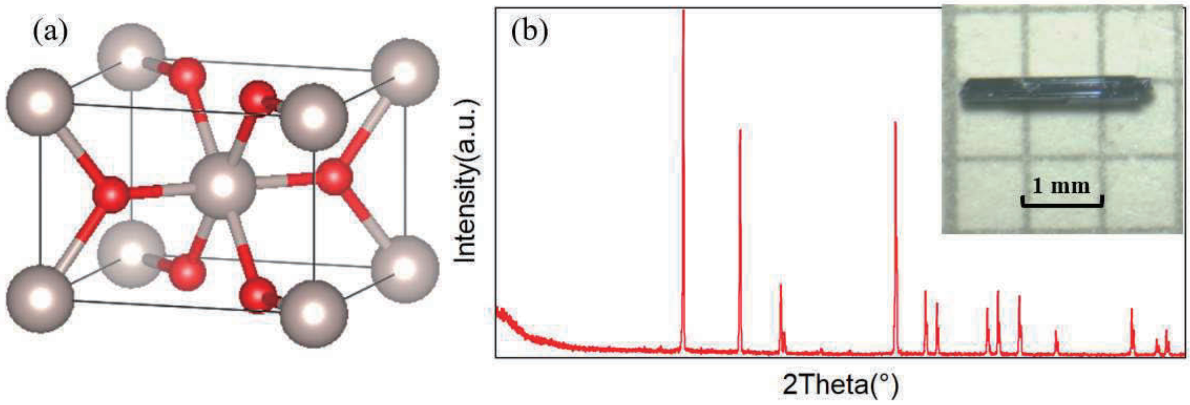

FIGURE 1. Crystal characterization of RuO_2 single crystal. (a) Crystal structure of RuO_2. (b) Powder x-ray diffraction data. Inset: Crystal against a millimeter grid.

RuO_2 is a collinear semimetallic antiferromagnet, with magnetic moment of ~0.05 μ_B per Ru atom and along the *c* axis. We have synthesized the samples by the chemical vapor transport method. Figure 1(b) shows our powder x-ray diffraction data and a photograph of the crystal.

We show the electronic band structure of RuO_2 obtained by angle-resolved photoemission spectroscopy at BL09B in Figure 2(a)-(d). We performed E-k maps at different photon energies and found that the E-k maps are not clear at this photon energy range. Since RuO_2 samples are not suitable to be measured at low photon energy, it is urgent to find other systems to verify this spin-splitting effect. Through theoretical analysis and He lamp ARPES measurement, we find that $MnTe_2$ and NiS_2 are systems with such antiferromagnetic spin splitting, which can be measured at low photon energies. Therefore, we believe that with subsequent support of BL09B, we can effectively discover this effect in such systems.

In addition, we measured Sb-doped $MnBi_2Te_4$ samples. Sb-doped $MnBi_2Te_4$ crystals were found to be magnetic topological insulators with sizable gaps in the topological surface state, and are considered to be a promising system to achieve high-temperature quantum anomalous Hall effect [7]. Through ARPES measurements, we resolved their surface states clearly, as shown in Figures 2(e)-(g). However, as magnetic domains smaller than the spot size are formed on the surfaces of Sb-MnBi$_2$Te$_4$, it is not easy to obtain reliable spin polarization signals, shown in Figures 2 (h).

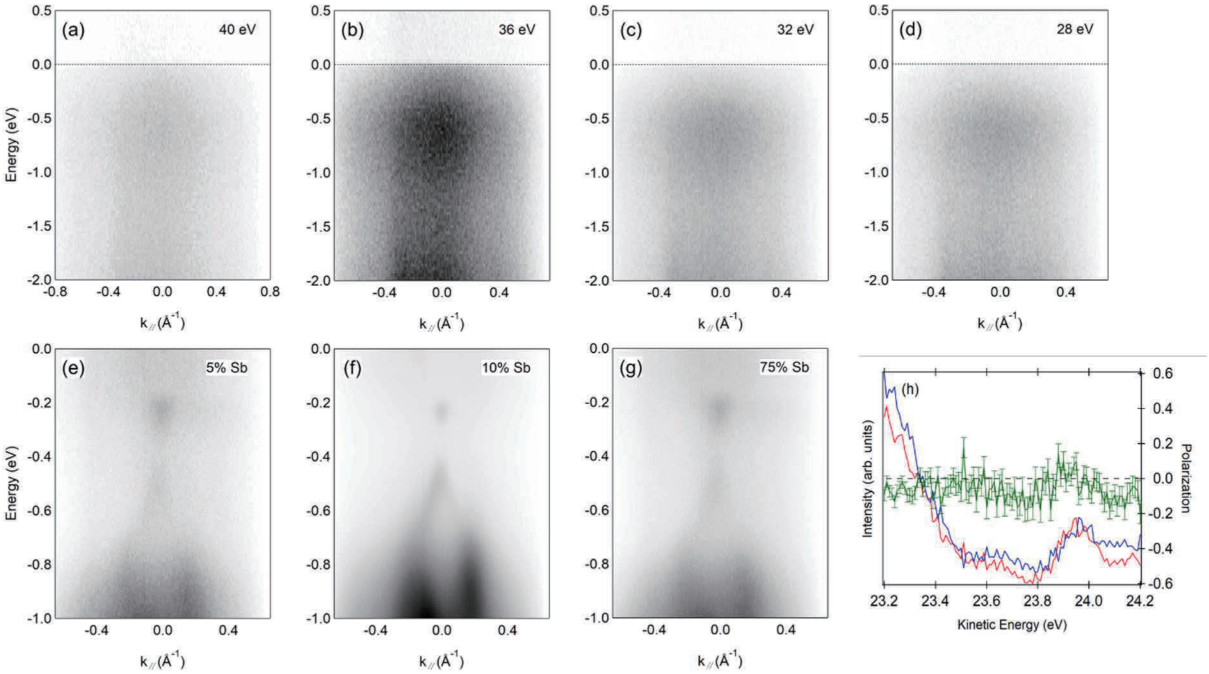

FIGURE 2. (a)-(d) E-k maps at 40 eV, 36 eV, 32 eV and 28 eV respectively. (e)-(g) E-k maps of MnBi$_{2-x}$Sb$_x$Te$_4$ for x=5%, 10% and 75% respectively. (h) In-plane spin-resolved energy distribution curves of spin up (red line) and down (blue line) obtained from k$_{//}$=0 Å^{-1} of MnBi$_{1.95}$Sb$_{0.05}$Te$_4$. Green lines show spin polarization as a function of kinetic energy.

REFERENCES

1. E. Rashba, et al., SvPhU **7**, 6 (1965).
2. G. Dresselhaus, et al., Physics Review **100**, 580 (1955).
3. S. Pekar et al., Zh. Eksperim. I Teor. Fiz. **47**, 1927 (1964).
4. A. Manchon et al., Physics **13**, 112 (2020).
5. L. Yuan et al., Physical Review B **102**, 014422 (2020).
6. L. Yuan et al. Physical Review Materials **5**, 014409 (2021).
7. X. Ma et al. Physical Review B **103**, L121112 (2021)

20AU017 BL-9B

Observation of Topological States in $Ca_2Pd_3Sb_4$ Superconductor

Shilong Wu[a, b], Kaito Shiraishi[d], Koji Miyamoto[c], Taichi Okuda[c], Gang Xu[e], Xingjiang Zhou[a]

[a]Beijing National Laboratory for Condensed Matter Physics,
Institute of Physics, Chinese Academy of Sciences, Beijing 100190, China
[b]University of Chinese Academy of Sciences, Beijing 100049, China
[c]Hiroshima Synchrotron Radiation Center, Hiroshima University, Higashi-Hiroshima, Hiroshima 739-0046, Japan,
[d]Graduate School of Science, Hiroshima University, Higashi-Hiroshima, Hiroshima 739-8526, Japan,
[e]Wuhan National High Magnetic Field Center & School of Physics, Huazhong University of Science and Technology, Wuhan 430074, China

Keywords: Topological superconductivity, SARPES.

The topological superconductors promise fabricating Majorana fermions, paving a pathway to braiding topology-protected qubits. However, topological superconductivity of iron-free stoichiometric pnicitides is rarely reported. Here, using spin- and angle-resolved photoemission spectroscopy and corresponding ab initio calculations, we have identified both bulk states and Dirac semimetal states near the Fermi energy in a superconducting $Ca_2Pd_3Sb_4$ pnicitide. The topological surface states on the (001) surface of $Ca_2Pd_3Sb_4$ right cross the Fermi level, while those of (100) surface pass through the Fermi level with slight electron doping, potentially allowing the coexistence of several topological states in the superconducting compound. These results reveal several topological surface states emerging in an iron-free pnicitide, broadening a class of materials as a promising platform for topological superconductivity.

In this proposal, we have studied the superconducting $Ca_2Pd_3Sb_4$ by the combination of spin- and angle-resolved photoemission spectroscopy (SARPES) experiments and ab initio electronic structure calculations. According to our ab initio calculations, $Ca_2Pd_3Sb_4$ is a class of pnichitides with nontrivial topological electronic band structures. Furthermore, an unpublished experiment has shown that the superconducting transition temperatures (Tc) of $Ca_2Pd_3Sb_4$ is 1.6 K. Here we only show the partial experimental results, firstly, comparatively determined the Fermi surface of $Ca_2Pd_3Sb_4$ with both p- and s- polarized synchrotron radiation as shown in Fig. 1.

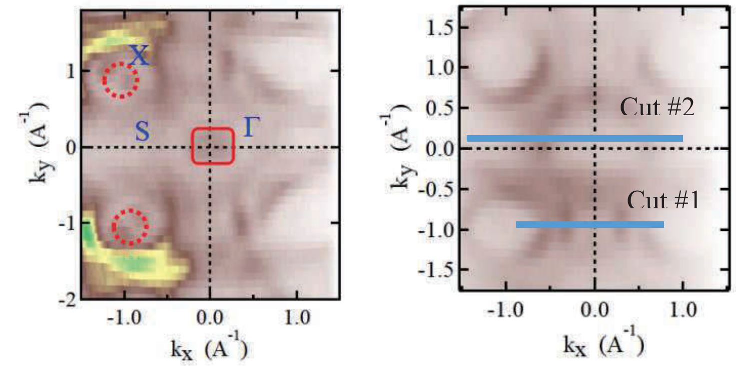

Figure 1.
(a) 70 eV and horizontal-polarized light
(b) 70 eV and vertical-polarized light

To examine our theoretical prediction of the nontrivial topological phase, we have carried out systematical ARPES measurements on the (001) cleavage surface of $Ca_2Pd_3Sb_4$ single crystals. We determined the momentum locations tangential to the sample surface by photon polarization dependent ARPES measurements. Figure 1(a) and (b) show the in-plane Fermi surfaces (FSs) measured with hv = 70 eV with p- and s-polarized synchrotron radiation which are consistent with the calculated FSs in planes, respectively. As seen in Fig. 1(a), by measuring with p-polarized light, the quasi-2D FSs have two circular contours around X point and rectangular contours around S point in the plane, the two circular contours consist with an outer circle and an inner semicircle around X point. Nevertheless, by measuring with s-polarized light, the inner semicircular contours are disappeared. Moreover, the rectangle-shape contours around Γ point is also unvisible with s-polarized light measurement. With comparison of our band structure calculations, the weight of rectangle-shape contours should be ascribed to topological surface states. However, because the beamtime is limited in two days, the high resolution band dispersion at Γ point is absent so far.

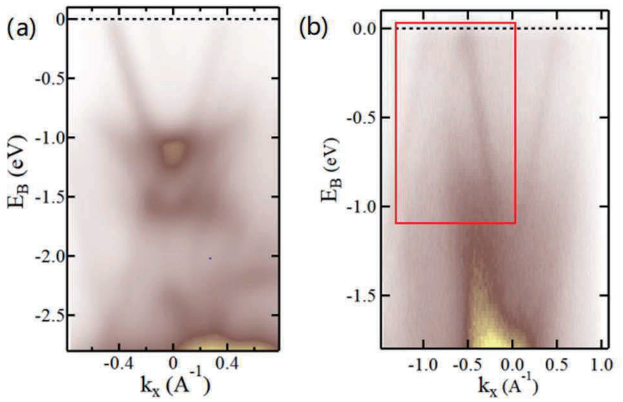

Figure 2.
(a) band dispersion along X-S-X line taken by 70 eV and horizontal light.
(b) band dispersion along S-Γ-S line taken by 70 eV and vertical light.

Figure 2(a) shows bulk electronic structures of $Ca_2Pd_3Sb_4$. We investigated band dispersions along X-S-X line and cut #1 in Fig. 2. The parabolic bands crossing the Fermi energy are ascribed to Ca $4s^2$ outermost shell electrons. Other bands come from antimony. They are consisted with band calculations around this point. According to spin resolved energy dispersion curves along cut #1, no spin polarization was observed, it indicates that the band structures at cut #1 can be ascribed to bulk band dispersion without surface contributions.

Figure 2(b) shows linear Dirac-like states at cut #2 and along S-Γ-S line which are remarkably different with calculated bulk band structures. As shown in the red box of Fig. 2(b), a Dirac-like band crossing is clearly resolved at ~10 meV below E_F along cut #2. These experimental data demonstrate that the Dirac-cone surface states could be located around projected X point of [001] surface. More efforts needed to be made to identified this Dirac-cone band dispersion from both calculations and experiments in the near future. In the last beamtime measurements, unfortunately, no spin resolved energy dispersion curves were performed at cut #2.

In conclusion, in two days beamtime of beamline 9B station, we can see that electronic structures around X point are well coincided with band calculations, but linear topological surface states at S point and Γ point emerge and can not ascribed to bulk states. In the next step, we can reveal the topological surface states by further SARPES measurements and band calculation.

REFERENCES

1. N. Read and D. Green, Phys. Rev. B 61, 10267 (2000).
2. L. Fu and C. L. Kane, Phys. Rev. Lett. 100, 096407 (2008).

20AG012 BL-11

Efficient photocatalytic activation of C-H bonds by spatially controlled chlorine and titanium on the silicate layer

Nao Tsunoji,[a] and Shinjiro Hayakawa,[a]

[a] *Graduate School of Advanced Science and Engineering, Hiroshima University,*

Keywords: photocatalysis • tianosilicate • layered silicate • cyclohexane • selective oxidation • C-H activation

The efficient activation and transformation of C(sp^3)-H bonds in alkanes to produce higher-value products remains one of the biggest challenges in modern chemistry. Such bonds are thermodynamically strong and kinetically inert, and molecular oxygen is an unreactive oxidant. Therefore, traditional catalytic strategies for their conversion require the use of expensive and aggressive reagents and/or severe reaction condition.

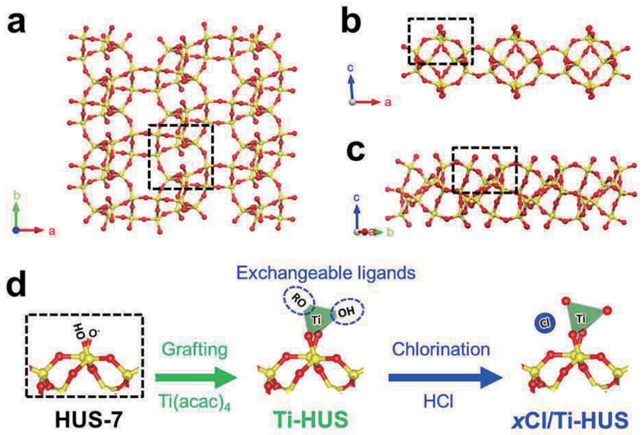

FIGURE 1. HUS-7 silicate framework viewed along the (a) c-axis, (b) b-axis, and (c) a-axis. The dotted squares indicate the repeating structural unit containing a silanol and a silanolate group. (d) Ti grafting and chlorination on the HUS-7silicate layer.

In the previous study, we selected two inorganic elements (chlorine and titanium) and developed highly efficient photo-driven organic transformations by accurate control of their spatial distribution.[1] Recently, we developed a rational design strategy for realizing isolated metal species on layered silicates. Layered silicates composed of anionic silicate sheets with interlayer cations are a kind of layered material whose interlayer surfaces are covered with silanol (SiOH) and silanolate (SiO^-) groups with crystallographically defined arrangements and bond angles.[2-5] We found that isolated titanium species with uniformly tetrahedral coordination states and high surface densities are provided by the grafting of titanium(IV) acetylacetonate onto the surface of a Hiroshima University silicate (HUS, Figure 1). As shown in Figure 1, further remarkable features of this material are the specific coordination environment of isolated species linked by two Ti−O−Si bridges and the presence of exchangeable ligands (acetylacetonate or hydroxyl groups). We attempted to incorporate chlorine at locations neighboring isolated titanium atoms by ligand exchange, yielding a chlorinated layered silicate catalyst. The C-H activation ability of the catalyst was evaluated in the photocatalytic oxidation of cyclohexane into its partially oxidized products cyclohexanone and cyclohexanol, which are important intermediates in the manufacture of nylon polymers. We also employed a chlorine-incorporating zeolite material (TS-1) and titanium oxide (P25) for comparison in order to assess the influence of the spatial distribution of the elements on the efficiency of the partial oxidation reaction.

In this study, to get further insight into the additional structural modification with different metal components (indium and palladium), their L-edge X-ray absorption spectroscopy (XAS) measurement was investigated (Figure 2). To determine the analysis condition of L-edge XAS measurement, palladium loaded titanium oxide (Pd@P25) and indium loaded titanium oxide (In@P25) were prepared by typical impregnation method and calcination. As reference materials, indium and palladium oxides were used. For the Pd L-edge measurement (Figure 2 left), the peak position of the material is roughly matched with the reference. However, the peak is quite narrow, indicating uniform environment around palladium atom. In contrast, the indium L-edge spectra between the sample and reference were similar although the pre-edge intensity was slightly different. From these observation, we have optimized the XAS measurement condition for palladium and indium L-edge. We are planning the further detailed structural analysis for the photocatalyst after screening the activity test.

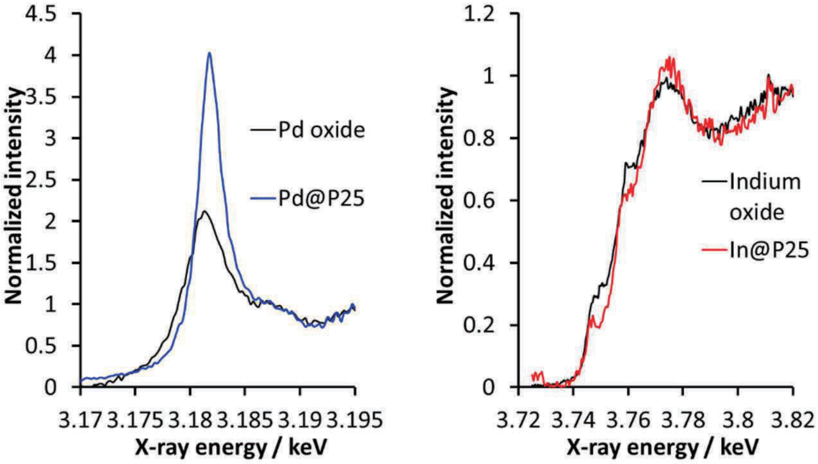

FIGURE 2. (left) Pd and (right) In L-edge XANES spectra for palladium oxide, Indium oxide, palladium loaded titanium oxide (Pd@P25) and indium loaded titanium oxide (In@P25).

REFERENCES

1. N. Tsunoji, H. Nishida, Y. Ide, K. Komaguchi, S. Hayakawa, Y. Yagenji, M. Sadakane, T. Sano, *ACS Catal.* **2019**, *9*, 5742-5751.
2. N. Tsunoji, T. Ikeda, M. Sadakane, T. Sano, *J. Mater. Chem. A* **2014**, *2*, 3372-3380.
3. N. Tsunoji, Y. Ide, Y. Yagenji, M. Sadakane, T. Sano, *ACS Appl. Mater. Interfaces* **2014**, *6*, 4616-4621.
4. N. Tsunoji, M. Bandyopadhyay, Y. Yagenji, H. Nishida, M. Sadakane, T. Sano, *Dalton Trans.* **2017**, *46*, 7441-7450.
5. N. Tsunoji, M. V. Opanasenko, M. Kubu, J. Cejka, H. Nishida, S. Hayakawa, Y. Ide, M. Sadakane, T. Sano, *ChemCatChem.* **2019**, *9*, 5742-5751.

20AG034 BL-11

Structure of a Novel Amorphous Organic-Inorganic Hybrid Tin Cluster Exhibiting Nonlinear Optical Effects by Low-Energy XAFS Measurements

Jens R. Stellhorn[a], Kazunori Yagi[a], Shinjiro Hayakawa[a], Benedict Paulus[b], Benjamin D. Klee[b], Wolf-Christian Pilgrim[b], Stefanie Dehnen[b]

[a] *Department of Applied Chemistry, Graduate School of Advanced Science and Engineering, Hiroshima University, Higashi-Hiroshima, Hiroshima 739-8527, Japan*
[b] *Department of Chemistry, Philipps University of Marburg, Marburg 35032, Germany*

Keywords: Amorphous structure, low-energy XAFS, non-linear optical effect

Tailored light sources have greatly advanced technological and scientific progress by optimizing colour and brilliance, improving energy efficiencies or the quantum properties of light. So called supercontinuum generators are premier examples for media with nonlinear optical (NLO) effects – far superior in some respects to other sources such as phosphorescent white light-emitting diodes (LEDs). However, unlike LEDs, most of these advanced light sources are only used for scientific purposes, as they require extreme electric field strengths which are commonly realized by high-power pulsed lasers. In contrast, the materials of interest for this research project represent a new generation of supercontinuum emitters that are readily obtained from ubiquitous resources in a simple synthesis.

These compounds are of the general composition Sn4S6R4 (R=Methyl, Phenyl, Naphtyl, Cyclopentadienyl) and exhibit strong NLO effects, making it possible to use them as cheap and efficient warm-white supercontinuum emitters when driven by a commercially available low-power continuous-wave infrared laser diode [1]. Quantum chemical calculations suggest that these compounds consist of Sn4S6 clusters. On the other hand, it was also confirmed that the NLO effect is linked to the amorphous nature of the materials, but the structural properties of the amorphous phase, and thereby the apparent origin of this effect, is difficult to determine [2].

Recent investigations indicate that the relative orientation of neighboring clusters comprise key information concerning the strength of the NLO effect.[3] These inter-cluster correlations can be probed by low-energy EXAFS measurements, which were conducted at BL11 for a sample with R=Methyl. The analysis is complicated by the multitude of different EXAFS paths, therefore a good resolution in

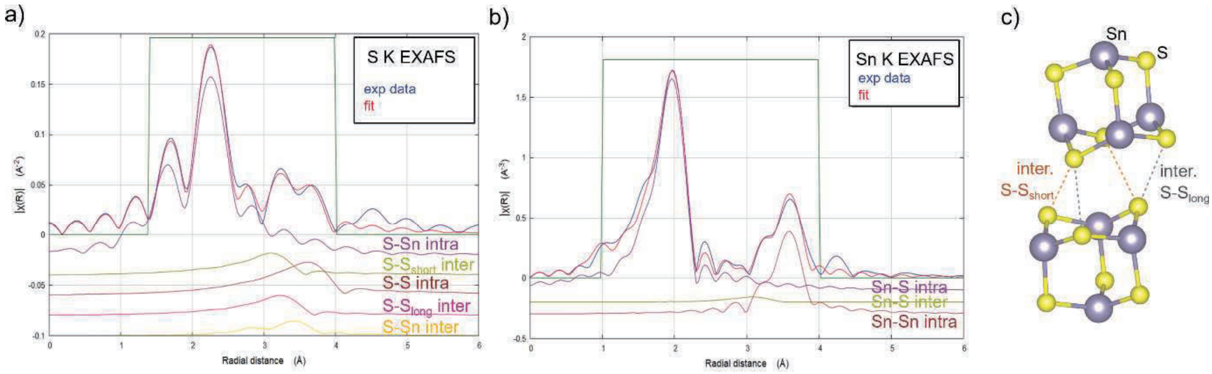

FIGURE 1. S K-edge EXAFS data (a) in comparison with Sn K-edge EXAFS data, and their fitting results. The model used for the fit is shown in (c), where the organic side groups are omitted for clarity.

real-space, corresponding to a wide *k*-range in the raw data, is essential. A simplified model based on the calculation of the dimer structure [3] gives a very good fit to the data (Fig. 1a) and is also in agreement with higher energy EXAFS data from the Sn K-edge (Fig. 1b). The model is illustrated in Fig. 1c, and comprises two different inter-cluster S-S distances, one short (about 3.70 Å) and one long (about 3.85 Å) distance.

The results indicate an inter-cluster S-S coordination number of 0.7, tantamount to a dimerization of the Sn4S6R4-clusters (expected CN is 0.66). A formation of a further network of arranged clusters (equivalent to a larger inter-cluster S-S coordination number) is demonstrated to be unlikely for the clusters with Methyl side groups. Further work is necessary to investigate samples with other organic side groups to reveal possible links between the network formation and the NLO effect.

REFERENCES

[1] N.W. Rosemann et al., Science 6291, 1301 (2016).
[2] B. D. Klee, et al., Phys. Stat. Solidi B 255, 1800083 (2018).
[3] K. Hanau et al., Angew.Chem. Int. Ed. 60, 1176-1186 (2021).

20AG049 BL-11

Polarization dependent sulfur K-edge XAFS measurements of P3HT thin films for determination of film orientations with the improved sensitivity

Haruka Yoshimoto, Jens R. Stellhorn, Kenji Komaguchi, Shinjiro Hayakawa

Graduate School of Advanced Science and Engineering,
Hiroshima University, Higashi-Hiroshima, Hiroshima 739-8527, Japan

Keywords: XAFS, conversion electron yield, angular dependence, P3HT

1. Introduction

X-ray absorption fine structure (XAFS) measurements in the soft X-ray region are widely conducted with a total electron yield (TEY) method under the vacuum owing to the difficulties in preparing samples of appropriate optical thickness for the transmission method, and the X-ray fluorescence yield (XFY) method is supplementary employed for other cases. We have been employing a conversion electron yield (CEY) method that utilizes the ionization of surrounding He gas molecule by the energetic Auger electrons from a sample. The CEY is advantageous in the sense of S/N compared to the XFY. However, the use of an electrode that prevents created electron-ion pairs from recombination has generally made the geometrical restrictions for angular dependent measurements. We have developed a new device that can make the angular dependent XAFS measurements using CEY method. And we report the results of determination of the orientation for P3HT thin films using the developed device.

2. Experimental

2.1 A CEY device

A principle of the CEY measurements is similar to that of X-rays with an ionization chamber except for the source of the gas ionization. Therefore, a planer electrode has been adopted in the experimental setup at BL11 [1]. To realize the angular dependent measurements we have developed a new device shown in Fig.1. The device is equipped with a rod-shaped electrode. The diameter of the electrode in the new device was 6 mm, and the relatively wide diameter of the anode has maintained the strength of the electric field within the region of the ionization chamber. The cross section of the anode was semicircle, and the electrodes are placed above and below the beam height.

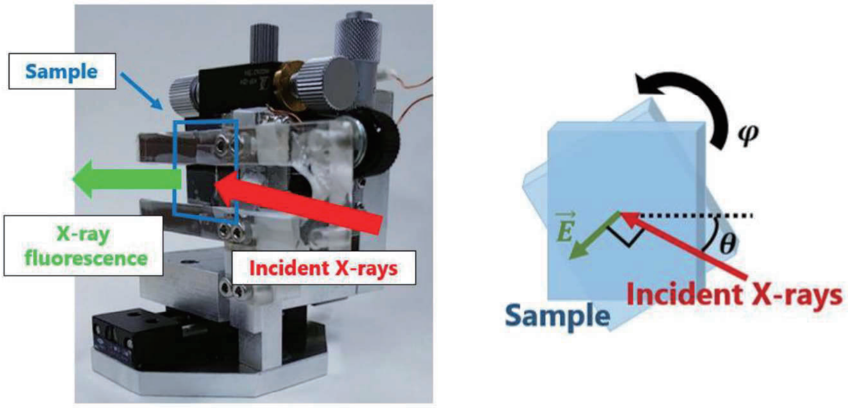

FIGURE 1. A photograph of the new device for the angular dependent CEY measurements (left), and a schematic layout of the sample geometry including glancing angle, θ and the azimuthal angle, φ (right).

2.2 XAFS measurements

XAFS measurements were performed at BL-11 of HiSOR. Incident X-rays were monochromatized with a Si(111) double crystal monochromator. The XFY was detected with a silicon drift detector (SDD) in a He filled chamber. A poly(3-hexylthiophene) (P3HT) film on ITO glass substrate was utilized as a sample having an anisotropy in sulfur K-edge XAFS spectra. A chlorobenzene solution of P3HT(Rieke Metals, Mw=58000) was spin-coated on a special ITO/glass substrate, and the surface of the substrate was previously brushed with a velvet fabric. The majority of backbones of edge-on oriented molecules are expected to be aligned in the brushing direction [2]. The azimuthal angle, φ was defined to be 0 when the electric field of the incident X-rays was normal to the brushing direction.

3. Results and Discussion

FIGURE 2 shows the azimuthal angle, φ dependence of S K-edge XAFS spectra from a P3HT thin film at θ = 80°. The 1s to π* peak (π*) showed strong peak under the condition of φ = 0 °. A plot of the intensities of π* peak is shown as a function of azimuthal angle (FIGURE 3). We consider a three-component system that includes edge-on orientation (uniaxial and random) and face-on as components of orientation. But the almost direct incidence condition suggests that the contribution from the face-on orientation of the molecules is negligible, and the obtained π* data can be attributed to molecules in the uniaxial edge-on direction and those in the random edge-on direction. This anisotropy could be expressed by the $\cos^2\varphi$ function. On the other hand, the azimuthal dependence of the σ*S-C peak (FIGURE 4) should include the contribution of molecules in the face-on orientations. As the anisotropy of the σ*S-C peak was originated from the molecules in the uniaxial orientation, analysis of these two curves enabled us to determine the fractions of three components, and the fraction of the uniaxial orientation (edge-on) was determined to be 35 %.

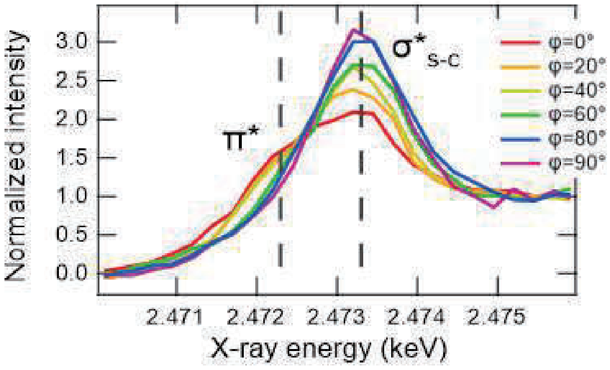

FIGURE 2. Azimuthal angle dependence of S K-edge XAFS spectra (θ=80°) from uniaxial edge-on oriented P3HT thin film.

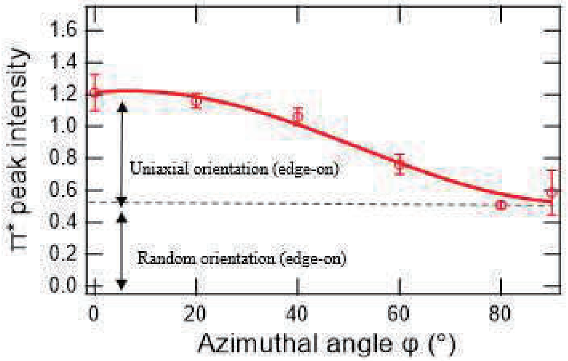

FIGURE 3. A plot of the π* peak intensities as a function of the azimuthal angle.

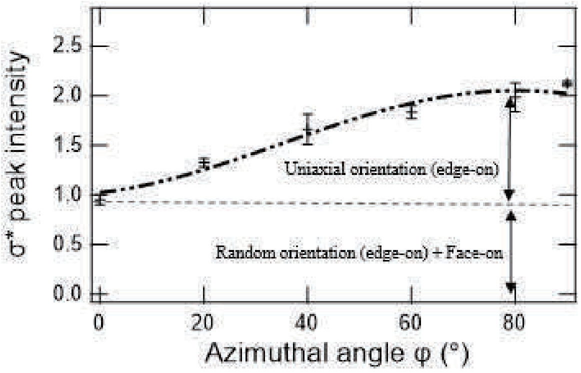

FIGURE 4. A plot of the σ* peak intensities as a function of the azimuthal angle.

References

[1] S. Hayakawa, Y. Hajima, S, Qiao, H. Namatame, T. Hirokawa, Anal. Sci., 24, 835(2008)
[2] M. Imanishi, D. Kajiya, T. Koganezawa, K. Saitow, Sci.Rep.**7,** 5141 (2017)

Evaluation Of The Self-healing Bio-assisted Cement-treated Clay With XAFS

Satoru Ikoma[a] ,Joyce Nakayenga[a],Toshiro Hata[a] and Shinjiro Hayakawa[b]

[a] *Department of Civil and Environmental Engineering, Graduate School of Engineering, Hiroshima,University, Higashi Hiroshima, Hiroshima, 739 8527, Japan*

[b] *Department of Applied Chemistry, Graduate School of Engineering, Hiroshima University, Higashi Hiroshima, Hiroshima, 739 8527, Japan*

Keywords: XAFS, Cement-treated clay, Calcium carbonate.

1. Introduction

Cement is one of the most widely used materials for ground improvement. Recently, there has been increasing interest in the durability / robustness of cement-treated soil. In the marine environment, cement-treated soil is deteriorated by the percolation of salt from seawater [1].

As a countermeasure to this phenomenon, self-mediated cement treated clay with biomineralization is proposed to enhance the durability of cement-treated clay against seawater [2]. In this study, the morphology were of the cement-treated soil with biomineralization based self-heling cement treated clay was analyzed using X-ray absorption fine structure (XAFS).

2. Chemical reaction for deterioration mitigation

Calcium hydroxide, an important cementation component of cement-treated soil, reacts with magnesium salts in seawater to form highly water-soluble calcium salts, which are leached into seawater (Eq.1-2) [1]. In cement-treated soil with Bacteria and urea, urea is hydrolyzed to produce carbonate ions by bacterial function (Eq.3) [2]. The calcium ions resulting from the deterioration are reacted with the carbonate ions derived from urea, and they are reprecipitated as calcium carbonate (Eq.4) [2]. The above chemical reaction equation is described below.

$$Ca(OH)_2 + MgCl_2 \rightarrow CaCl_2 + Mg(OH)_2 \qquad \text{(Eq.1)}$$

$$CaCl_2 \rightarrow Ca^{2+} + 2Cl^- \qquad \text{(Eq.2)}$$

$$CO(NH_2)_2 \rightarrow \text{urease} \rightarrow 2NH^{4+} + CO_3^{2-} \qquad \text{(Eq.3)}$$

$$Ca^{2+} + CO_3^{2-} \rightarrow CaCO_3\downarrow\text{(precipitation)} \qquad \text{(Eq.4)}$$

3. Experimental method

Ordinary Portland cement was added to the marine clay and mixed. This sample was named "Sample A". "Sample B" was prepared by mixing urease-producing bacteria (*Sporosarcina aquimarina*) and urea to mixtures produced similarly to sample A. The samples at this point were used as the initial samples. These samples were filled into a mold and cured under sealed conditions. After curing, the specimens were exposed to 150 mL of artificial seawater for 196 days with only the top surface open. A sample of 5 mm was taken from the exposed surface of the specimen after exposure. The samples were dried in an oven at 105°C until there was no change in mass, and then finely ground using a mortar. In addition, samples of special reagent grade were prepared to simulate calcium hydroxide which are important cementation components of cement-treated soil and bacterial calcium carbonate, respectively.

XAFS measurements were performed at BL-11 of the Hiroshima Synchrotron Radiation Center (HiSOR) with the conventional transmission mode without calibrating the incident Xray energy.

4. Results and discussion

FIGURE 1 shows the XAFS spectra of samples and reference materials. Focusing on the reference samples, the peak of calcium hydroxide was observed at 4068 keV. Calcium carbonate (calcite), however, showed two peaks at 4066 keV and 4078 keV.

Both the initial samples showed peaks at 4068 keV, and the waveform was similar to that of the calcium hydroxide standard. For sample A (exposure), the peak was identified at 4068 keV, which was similar to that of initial sample. In sample B, a spectrum similar to calcite was obtained after exposure.

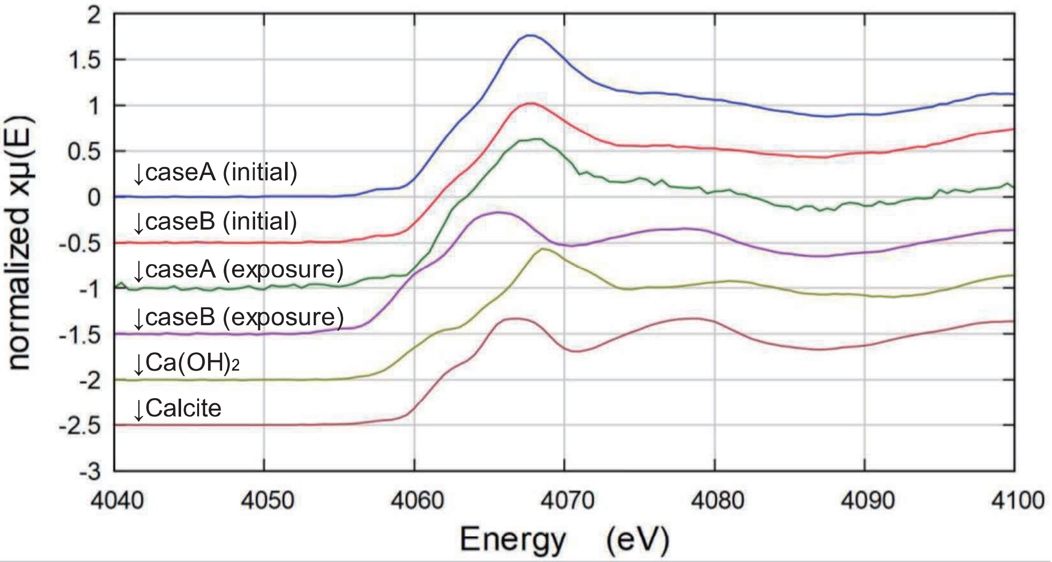

FIGURE 1 Calcium K-edge XAFS spectra of samples and reference materials

Based on these results, fractions of calcium hydroxide and calcite in the samples A and B were calculated using the spectra sum of reference materials. TABLE 1 shows the calculated results at the initial and the exposure stages. Before the exposure, both samples were found to be mainly composed of calcium hydroxide. After the exposure, sample B was almost completely converted to calcite. Calcium carbonate shows different structures depending on the type of urease-producing bacteria used as biocatalysts. Previous study where TG-DTA analysis was used, has shown that the calcium carbonate precipitated by *Sporosarcina aquimarina* is mainly calcite based, and our results strengthen the results of previous study [3].

TABLE 1 Calculated fractions of calcium hydroxide and calcite in unknown samples.

Sample name	**$Ca(OH)_2$**	**$CaCO_3$(Calcite)**
Sample A(initial)	0.756	0.244
Sample A(exposure)	0.541	0.459
Sample B(initial)	0.751	0.249
Sample B(exposure)	0.190	0.810

5. Conclusion

In this study, the authors used XAFS analysis to investigate the structure of the crystals formed in cement-treated clay mixed with urease-producing bacteria when it comes into contact with seawater. The results showed that most of the calcium hydroxide was converted to calcium carbonate by the microbial function in the sample exposed to seawater, while the calcium hydroxide was the main component in the sample before exposure. Moreover, calcium carbonate turned out to be calcite.

REFERENCES

1. H. Hara, D. Suetsugu, S. Hayashi, Y. J. Du. “Calcium leaching properties of lime-treated soil by infiltration of tidal river water” in *Proceedings of the International Offshore and Polar Engineering Conference*, Vancouver, Canada,810-813.
2. S. Ikoma, T. Hata, M. Yagi, T. Senjyu., *Environmental Geotechnics*, 2020.
3. A. Clarà Saracho, S.K. Haigh, T. Hata, K. Soga, S. Farsang, S.A.T. Redfern, E. Marek., *Sci Rep*. **10**, 10168, 2020.

Degradation Analysis of Automotive Oil with ZnDTP Additive by Fluorescence yield XAFS method

Susumu MINEOI[a], Kenjiro MOMOSAKI[b], Hirosuke SUMIDA[b],
Shinjiro HAYAKAWA[c]

[a]*Advanced Automotive Research Collaborative Laboratory, Graduate School of Advanced Science and Engineering, Hiroshima University, 1-4-1 Kagamiyama, Higashi-Hiroshima 739-8527, Japan*
[b]*Technical Research Center, Mazda Motor Corporation, 3-1 Shinchi, Fuchu-cho, Aki-Gun 730-8670, Japan*
[c] *Graduate School of Advanced Science and Engineering, Hiroshima University, 1-4-1 Kagamiyama, Higashi-Hiroshima 739-8527, Japan*

Keywords: oil, zinc dialkyldithiophosphate (ZnDTP), sulfur, XAFS.

Automotive oils play important roles such as transmitting pressure, reducing wear on sliding parts, cooling parts and cleaning surfaces of parts in maintaining the long-term quality of automobiles. Therefore, automotive oils should be selected properly according to automotive component specifications. In automotive oils, various additives are used to improve required functions while preventing degradation of the base oils. Zinc dialkyldithiophosphates (ZnDTP) are additives used to reduce wear of sliding parts by forming protective films on the part surface. The function of wear reduction is gaining more important to withstand hard wear because of the downsizing of mechanical parts for lightweighting. In this study, we investigated the heating-induced alteration of ZnDTP in an engine oil by using X-ray absorption fine structure (XAFS) method.

Commercial 0W-20 engine oil with ZnDTP additive was used as an oil sample. The oil was placed in glass watch dishes and heated under ambient atmosphere at 200°C for up to 40 hours in an electric furnace. A series of heated oil was directly dropped onto filter papers of chemical analysis grade (ADVANTEC TOYO KAISHA, LTD.). Octasulfur (Chemicals Evaluation and Research Institute, Japan) and tetramethylthiuram monosulfide (Tokyo Chemical Industry Co., Ltd.) were used as reference samples. Chemical state of sulfur in ZnDTP molecular was investigated using XAFS measurement system at HiSOR BL11 with the X-ray fluorescence method. A sample was placed in a Helium filled sample chamber during the XAFS measurement. The XAFS spectra of oil samples were acquired with the X-ray energy range from 2460 to 2490 eV with the interval of 0.25eV. The XAFS measurements were repeated 4 times, and the obtained spectra were averaged after the normalization with the incident beam intensity. The incident X-ray energy was calibrated so that the main peak energy of potassium sulfate ($CaSO_4$) was 2481.6 eV.

Figure 1 shows sulfur K-edge XAFS spectra of an oil sample, octasulfur and tetramethylthiuram monosulfide. The peak energy of the oil spectrum was 2472 eV, and it was almost identical to that of octasulfur. The chemical state of the sulfur in the ZnDTP might be similar to that of octasulfur.

Figure 2 shows the sulfur K-edge spectra of the oil samples as a function of heating time. As mentioned previously the initial peak position was close to that of octasulfur, and the peak might be attributed to transition from 1s to σ^*(sulfur-zinc or sulfur-phosphorous) similar to σ^*(sulfur-sulfur, sulfur-carbon) of sulfur-containing molecules [1-4]. It is clear that the main spectral features of the initial sample disappeared after 16 hours of heating, and a new peak was observed at 2482eV. This peak energy is close to those of sulfonate (SO_3^{2-}) or sulfate (SO_4^{2-}) [1, 2]. The spectral transformation indicated that the ZnDTP was oxidized in the early stage of the heating, although the oils were heated under its temperature limit. To prevent undesired reaction of ZnDTP with oxygen and retain ZnDTP in the oil for reforming protective films, adequate amount of antioxidant will be required in the oils.

The future investigations, of automotive oils with different additive blends will clarify the combined effects of additives for maintaining the long-term quality of automobiles.

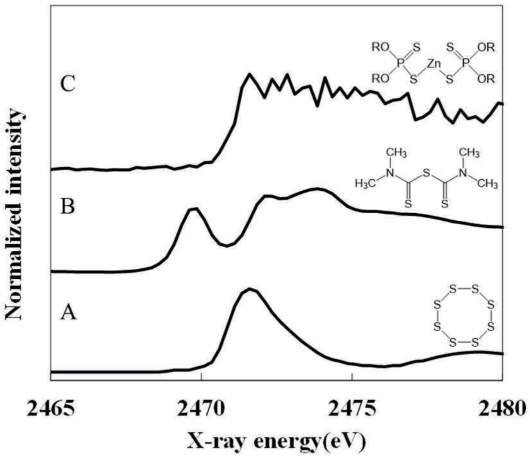

FIGURE 1. Sulfur K-edge XAFS spectra, A: octasulfur, B: tetramethylthiuram monosulfide, C: oil sample with ZnDTP additive (unheated).

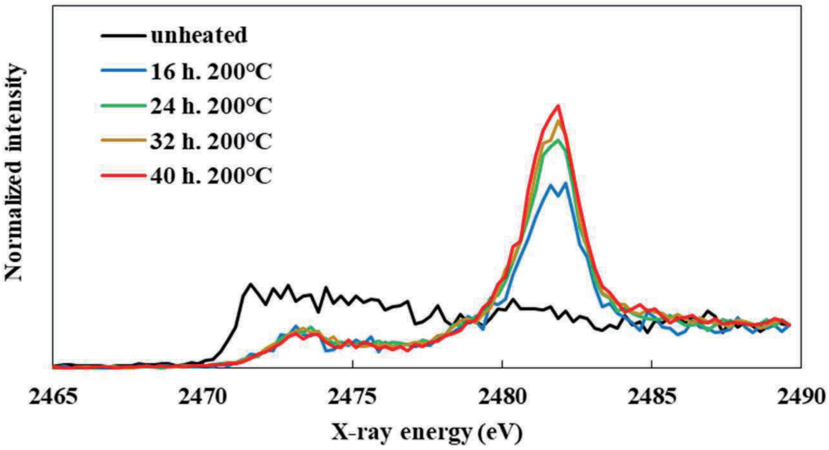

FIGURE 2. Sulfur K-edge XAFS spectra of oil samples as a function of the heating time.

REFERENCES

1. J. Prietzel et al., *Environ. Sci. Technol.* 45, 2878 (2011)
2. K. Takemoto et al., J. Water Environ. Technol., 14, 82(2016)
3. R.Chauvistré et al., Chemical Physics, 223, 293(1997)
4. H.Modrow et al., RUBBER CHEM. TECHNOL. 74, 281(2001)

20AG051, 19AG026 BL-12

Effects of Mono-Saccharides on Structural Stabilization of Apo-Myoglobin Studied by Synchrotron-Radiation Circular-Dichroism Spectroscopy

Takeru Shimizu[a], Ayano Uomi[b], Munehiro Kumashiro[a], Yudai Izumi[c], and Koichi Matsuo[c]

[a]*Department of Physical Science, Graduate School of Science, Hiroshima University, 1-3-1 Kagamiyama, Higashi-Hiroshima, Hiroshima 739-8526, Japan*
[b]*Faculty of Science, Hiroshima University, 1-3-1 Kagamiyama, Higashi-Hiroshima 739-8526*
[c]*Hiroshima Synchrotron Radiation Center, Hiroshima University,*
2-313 Kagamiyama, Higashi-Hiroshima, Hiroshima 739-0046, Japan

Keywords: apo-myoglobin, circular dichroism, denaturation, saccharide, structural stability

Structures of proteins sensitively change depending on the solvent environments, affecting those biological functions and physical properties. It is well known that the denaturations of proteins are induced by the increase in temperature and the decrease in pH but these can be prevented in the presence of co-solvents such as polyols and saccharides [1, 2]. However, the stabilization mechanism is complicated and still unclear. In this study, structural changes of apo-myoglobin (aMb) in the heat- and acid-denaturations in the presence of D-glucose (glc) and D-xylose (xyl) was observed using synchrotron-radiation circular-dichroism (SRCD) spectroscopy to discuss the effect of the molecular properties of the mono-saccharides on the stabilization of aMb structure.

Figure 1 shows the SRCD spectra of aMb at native (N) and acid-denatured (A) states in the presence or absence of glc and xyl. The N-state spectrum showed the helical rich conformation (helical content: 40.5%) but the A-state exhibited the characteristic peaks of unordered structure and included a small amount of helical structure (helical content: 4.5%). When adding glc and xyl, the spectra exhibited negative peaks around 222 and 208 nm and a positive peak around 190 nm, increasing the helical content (23.4% for glc and 17.3% for xyl), suggesting that the both mono-saccharides could contribute to the structural stabilization of aMb. We found small differences in the helical contents in the presence of glc and xyl. The difference in thier configurations is the presence of the hydroxymethyl group, indicating that this group would contribute as a factor for inhibiting the acid-denaturation of aMb. The SRCD spectra of aMb in the presence of methyl-α-D-glucopyranoside (Me-α-glc) and methyl-β- D-glucopyranoside (Me-β-glc) were also measured at the A-state. The helical contents in the both mono-saccharides decreased compared to the case of glc, suggesting that the hydroxy part of hydroxymethyl group might contribute to the stabilization of aMb structure. The effect of mono-saccharides on the heat-denaturation was also investigated

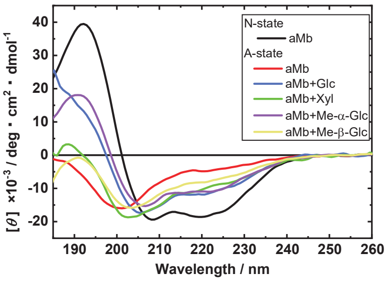

Figure 1 SRCD spectra of aMb in the presence of mono-saccharides.

in the temperature range from 10 to 94°C. As observed in the acid denaturation, it was expected that the hydroxy part of the hydroxymethyl group would enhance the structural stability.

Further data accumulation such as the cases in di- and oligo-saccharide solutions would be necessary to understand the relationships between saccharide structures and protein stability. The SRCD spectroscopy coupled with the heat- and acid-denaturation studies would be a useful tool for elucidating the contributions of the molecular properties of saccharides to the structural stabilization of proteins.

References

[1] T. Kamiyama, T. Marutani, D. Kato, T. Hamada, K. Kato, T. Kimura., J. Therm. Anal. Calorim. **123** (2016) 1861-1869.
[2] J. F. Back, D. Oakenfull, M. B. Smith., Biochem. **18** (1979) 5191-5196.

Study of Membrane-Bound Conformation and Pore Formation of Magainin2 using Vacuum-Ultraviolet Circular-Dichroism Spectroscopy

Ryoga Tsuji[a], Munehiro Kumashiro[b], Kouichi Matsuo[c]

[a]*Department of Physics, School of Science, Hiroshima University,*
1-3-1 Kagamiyama, Higashi-Hiroshima, Hiroshima 739-8526, Japan
[b]*Department of Physical Science, Graduate School of Science, Hiroshima University,*
1-3-1 Kagamiyama, Higashi-Hiroshima, Hiroshima 739-8526, Japan
[c]*Hiroshima Synchrotron Radiation Center, Hiroshima University, 2-313 Kagamiyama,*
Higashi-Hiroshima, Hiroshima 739-0046, Japan

Keywords: Antimicrobial Peptide, Lipid membrane, Circular dichroism

Magainin2 (MG2) is an antimicrobial peptide consisting of 23 amino acids, and its antimicrobial activity occurs due to the interaction with membranes followed by the formation of transmembrane pores. The activity closely relates to the membrane-bound conformation of MG2 and it largely depends on the characteristics of constituents of membrane or lipid molecules. Recently, it found that the characteristics such as the void-space within membrane and the fluidity of membrane contribute to the membrane interaction of proteins [1, 2]. Hence, to clarify the contribution of these membrane characteristics to the MG2-membrane interaction, the membrane-bound conformations of MG2 in the presence of four types of membranes which were prepared from DLPC, DMPC, DPPC, or DSPC lipid molecules were analyzed by a vacuum-ultraviolet circular dichroism spectroscopy.

MG2 formed a random coil structure in native state (without membrane) and its structure altered the helical structure in the presence of DLPC and DMPC lipid membranes at 25°C (**Figure 1**), meaning that MG2 interacted with the both membranes. On the other hand, MG2 retained its random coil structure in the presence of DPPC and DSPC lipid membranes, implying non-interaction. Since the phase transition temperature (T_m) of these lipid molecules are -2°C for DLPC, 24 °C for DMPC, 41 °C for DPPC, and 55 °C for DSPC, it was suggested that MG2 could interact with the membrane of liquid state. To enhance the fluidity of DPPC and DSPC lipid membrane or to get their liquid states, the temperature was raised above T_m of the both lipid molecules. After decreasing the temperature until 25°C, we found that MG2 formed helix structure in the DPPC lipid membrane but retained the random structure in the DSPC lipid membrane. The differences of DPPC and DSPC lipid molecules were their spontaneous curvatures (positive for DPPC and negative for DSPC), which affected the void-space within membrane (internal void-space for DPPC and external void-space for DSPC). Since DLPC and DMPC lipid membranes had the internal void-space, the internal space would be key factor for promoting the membrane-interaction of MG2.

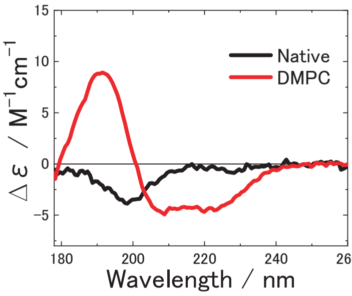

FGURE1 VUVCD spectra of MG2 in the presence and absence of DMPC lipid membrane at 25°C.

These results suggest that the internal void-space in membrane and the increment in the membrane fluidity would be one of the driving forces of MG2-membrane interactions.

REFERENCES

1. E. Strandberg, J. Zerweck, P. Wadhwani, and A. S. Ulirich, *Biophysical Journal*, March 2013, pp. L09-L011
2. L. Ma, Y. Luo, Y-H. Ma and X. Lu, *Langmuir,* 2021, 37, 1613-1621

20AG040 BL-12

Effect of Concentration on the Thermal Denaturation of Collagen

Yasuyuki Maki[a] and Koichi Matsuo[b]

[a] *Kyushu University, Fukuoka 819-0395*

[b] *Hiroshima Synchrotron Radiation Center, Hiroshima University, Higashi-Hiroshima 739-8526*

Keywords: Collagen, Denaturation, Vacuum-ultraviolet circular dichroism.

Collagen is the major protein found in extracellular matrices. The native collagen assumes well-known triple-helix structure. At temperatures higher than the melting temperature T_m, collagen is denatured and transition from helix to random coil occurs. The denaturation of collagen is a biologically important phenomenon because it occurs at temperatures near-physiological temperatures. The measurement of T_m is usually performed with dilute solutions of solubilized collagen. The effect of concentration on T_m for non-dilute collagen solutions at concentrations higher than the overlap concentration C^* has not been studied. The value of C^* of collagen is estimated to be 0.03 wt%, according to the relation $C^* = (M/N_\mathrm{A})/(4\pi\langle S^2\rangle^{3/2}/3)$, where M, $\langle S^2\rangle$, and N_A is the molecular weight, the mean square radius of gyration, and the Avogadro number. In the present study, the denaturation of collagen in non-dilute solutions at concentrations in the range between 0.05 wt% and 0.5 wt% was investigated using vacuum-ultraviolet circular dichroism (VUVCD) spectroscopy, which is an effective tool for analyzing structural change of proteins.

Collagen from porcine skin (NMP Collagen PS, Nippon Meat Packers, Inc., Japan) and atelocollagen from bovine skin (AteloCell IPC-50, Koken Co., Ltd, Japan) were used without further purification. The sample solutions were prepared by dissolving them in 1 mM HCl or 20 mM acetate buffer at pH 4. The $\mathrm{CaF_2}$ optical cell with 50, 100, and 400 μm path length was used for the collagen solution at the concentration of 0.5, 0.25, and 0.05 wt%, respectively. The VUVCD spectra were measured from 263 to 200 nm at temperatures from 10 °C to 60 °C under a nitrogen atmosphere using the synchrotron-VUVCD spectrophotometer of Hiroshima Synchrotron Radiation Center (BL-12) [1,2].

The VUVCD spectrum measured at 10 °C showed a positive peak at 221 nm, which is attributed to the triple-helix structure of the native collagen. The value of ellipticity θ at 221 nm decreased with temperature. The ellipticity for the native collagen θ_n and that for the denatured collagen θ_d were determined by the extrapolation of the plot of θ versus temperature T. The amount of helix χ of collagen was estimated by the equation: $\chi = (\theta - \theta_\mathrm{d})/(\theta_\mathrm{n} - \theta_\mathrm{d})$.

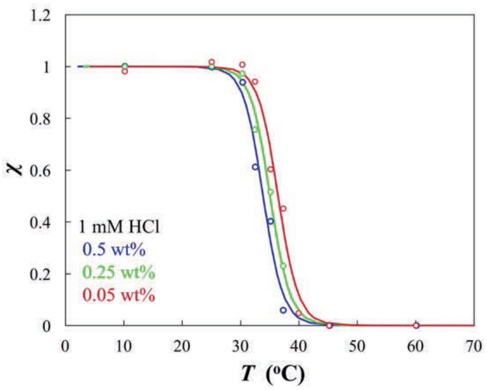

FIGURE 1. The plot of χ versus T for 0.05 (○), 0.25 (○) and 0.5 wt% (○) solutions of porcine skin collagen in 1 mM HCl.

Figure 1 shows the plot of χ versus T for 0.05, 0.25 and 0.5 wt% solutions of porcine skin collagen in 1 mM HCl. In Fig. 1, denaturation of collagen seems to occur at lower temperatures for higher collagen concentrations. The concentration dependence of T_m was significant for porcine skin collagen in 1 mM HCl and was not observed for the solutions of porcine skin collagen in acetate buffer and bovine skin atelocollagen in 1 mM HCl (Fig. 2). The mechanism for this strange concentration-dependent T_m of porcine skin collagen in 1 mM HCl is not clear at this time. The present study implied that the telopeptide region, which is absent in atelocollagen, had some role in the collagen denaturation.

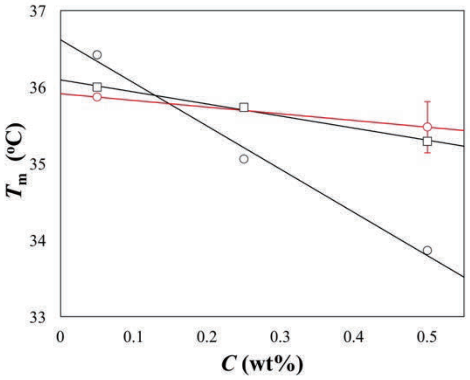

FIGURE 2. The plot of T_m versus concentration C for porcine skin collagen in 1mM HCl (○), porcine skin collagen in acetate buffer (□), and bovine skin atelocollagen in 1 mM HCl (○).

REFERENCES

1. K. Matsuo, K. Sakai, Y. Matsushima, T. Fukuyama and K. Gekko, *Anal. Sci.* **19**, 129-132 (2003).
2. N. Ojima, K. Sakai, K. Matsuo, T. Matsui, T. Fukazawa, H. Namatame, M. Taniguchi and K. Gekko, *Chem. Lett.* **30**, 522-523 (2001).

19AG030, 19BG005, 20AG038 BL-13

Electronic Relaxation Process in Fluorinated Aromatic Monolayers Studied by Core-Excited Ion Desorption

Kamon Yamamoto[a] and Shin-ichi Wada[b,c]

[a]*Graduate School of Science, Hiroshima University, Higashi-Hiroshima 739-8526, Japan*
[b]*Graduate School of Advanced Science and Engineering, Hiroshima University, Higashi-Hiroshima 739-8526, Japan*
[c]*Hiroshima Synchrotron Radiation Center, Hiroshima University, Higashi-Hiroshima 739-0046, Japan*

Keywords: Self-assembled monolayers (SAMs), Resonant core-electron excitation, Site-selective bond breaking, Ion desorption, Molecular conductivity

Core-electrons are localized to each atom in the molecule, and their binding energy varies depending on the types of element and the surrounding chemical environment. Therefore, by selecting the energy of the incident light, it is possible to selectively excite the inner-shell electrons of specific atoms in the molecule. After core resonant excitation, various reaction pathways occur (Figure. 1). Desorbed ions include site selective ion desorption (red arrow) and non-selective ion desorption through energy redistribution within the molecule (blue arrow). In the case of surface molecules, these reactions compete with energy deactivation by charge transfer to substrate (green arrow), so the faster the charge transfer to the substrate occurs, the more the slower reactions are suppressed. Site non-selective ion desorption is slower than site selective ion desorption. So, we tried to evaluate the charge transfer rate from the site selectivity of ion desorption.

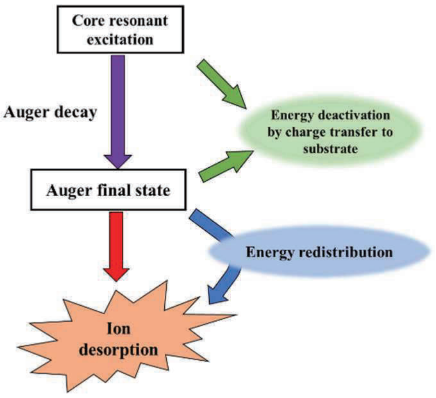

Figure 1. Reaction pathways after core resonant excitation.

Measurements of near edge X-ray absorption fine structure (NEXAFS) were performed at the beamline BL-13 of HiSOR, and time of flight (TOF) mass spectroscopy was measured at the beamline BL-2B of KEK-PF. NEXAFS spectra around the C K-edge were recorded in total electron yield (TEY) mode by measuring a sample drain current. TOF spectra were measured with pulse selector [1] in the hybrid mode operation at PF.

Figure. 2 shows the schematic drawings of self-assembled monolayers (SAMs) used in this study. SAMs were prepared by immersing Au substrates into 1.0 mM ethanol solutions of MBB ($HSC_6H_4C_6H_4COOCH_3$), MBF ($HSC_6F_4C_6H_4COOCH_3$), and MFB ($HSC_6H_4C_6F_4COOCH_3$). It has been reported that these samples have different charge transfer rate [2]. All samples have methyl ester groups as terminal groups at topmost surfaces, and conductive phenyl rings as molecular chains.

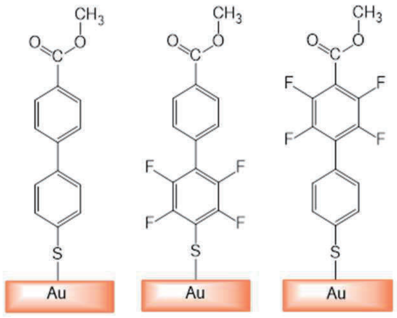

MBB MBF MFB

Figure 2. Molecular structures of SAMs used in this study; MBB, MBF, and MFB SAMs.

Figure 3 shows the NEXAFS spectra measured for MBF and MFB changing the incident angle. NEXAFS spectra show features derived from fluorine substitution, especially in the peak splits of the first (~285eV) and second peaks(~288eV). From the intensity of first peaks, MBF and MFB were estimated to be oriented at 74° and 69° from the surfaces, respectively. Even though the orientation angles of MBF and MFB are almost the same, the ion fragmentation in MFB is more intense than that in MBF in terms of its CH_n^+ (n=0-3) ion desorption yield. These ions are produced by further fragmentation of CH_3^+ due to the excess energy it has when it is desorbed from the terminal group. The excess energy in MFB is estimated to be higher than that in MBF. We estimated the ratio of site selective vs. non-selective processes by reproducing the ion fragmentation pattern by adding together the site selective and non-selective model fragmentation patterns. As a result, selective:non-selective ratios were 0.81:0.19 for MBF and 0.98:0.02 for MFB. The results show non-selective ion desorption in MFB is more restrained than that in MBF because energy deactivation by charge transfer to substrate in MFB is faster than that in MBF. This result is consistent with the charge transfer rate in MBF and MFB (MBF: ~8.8fs, MFB: ~6.6fs) [2]. Therefore, the difference in conductivity depending on the fluorine substitution position was evaluated from the site selectivity of ion desorption.

REFERENCES

1. H. Tanaka, J. Adachi, K. Otaki, M. Imai, H. Ishii, T. Kosuge, *KEK Proceedings*, 2019-9, 2019, pp. 22-26.
2. Y. Iyobe, A. Hiraya, S. Wada, *HiSOR Activity Report 2018*, 2019, pp.111-112.

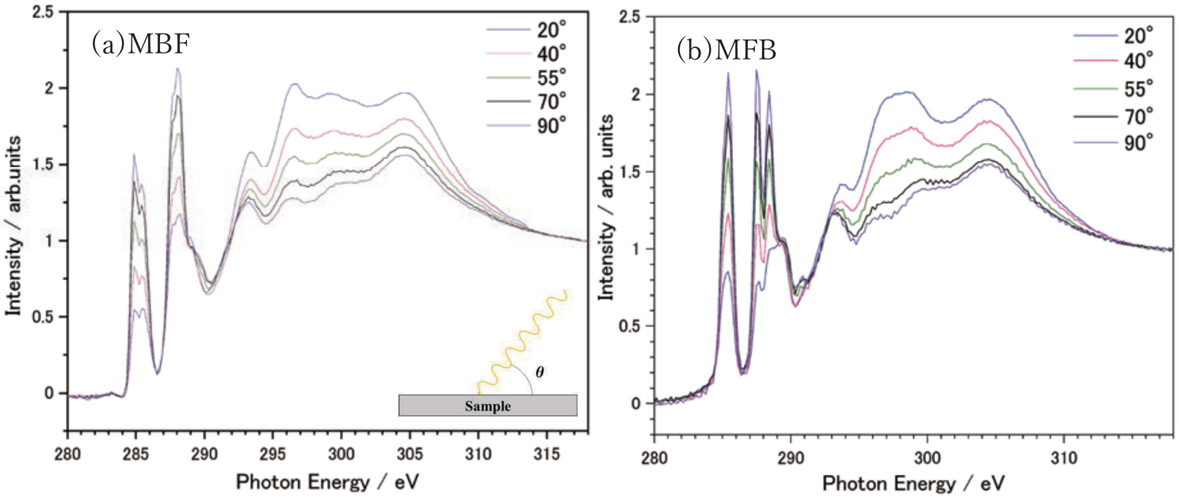

Figure 3 TEY spectra for (a)MBF and (b)MFB. The angles in the figure are the incident angles from the sample surfaces. MBF and MFB were estimated to be oriented at 74° and 69° from the surfaces, respectively.

20AG037, 20AG038 BL-13

Inner Shell Excitation Spectroscopy of Gold Nanoparticles Coated with Aromatic Molecules

Shogo Tendo[a], Yuki Okada[b], and Shin-ichi Wada[c,d]

[a] *Graduate School of Science, Hiroshima University, Higashi-Hiroshima 739-8526, Japan*
[b] *Faculty of Science, Hiroshima University, Higashi-Hiroshima 739-8526, Japan*
[c] *Graduate School of Advanced Science and Engineering, Hiroshima University, Higashi-Hiroshima 739-8526, Japan*
[d] *Hiroshima Synchrotron Radiation Center, Hiroshima University, Higashi-Hiroshima 739-0046, Japan*

Keywords: Self-assembled monolayers (SAMs), Gold nanoparticles, Laser ablation, Resonant core-electron excitation

Gold nanoparticles have been used commercially since the 4th century B.C. Gold nanocolloid solutions have a reddish purple color [1]. On the research front, it was found that organic molecules with thiol groups chemisorb onto the gold surface to form self-assembled monolayers (SAMs) in 20th century [2]. In recent years, next-generation materials and in vivo sensors based on gold nanoparticles modified with organic molecules have been developed. A lot of knowledge has been obtained about aliphatic SAMs. On the other hand, aromatic SAMs, which are expected to be applied as conductive materials, have not been fully understood. In this study, we compared the core excitation spectra of aromatic SAMs adsorbed on gold with different surface geometries and investigated the molecular states of the nanoparticle surface.

In this experiment, methyl 4-mercaptobenzoate (MP0) molecules with a methyl ester group (CH_3COO-) were used (Figure 1a). MP0-coated gold substrates (MP0S, Figure 1b) were prepared by immersing gold substrates in MP0 solution. The gold nanocolloid solution prepared with pulsed laser ablation in liquid (PLAL) technique. MP0-coated gold nanoparticles (MP0N, Figure 1c) were produced by adding MP0 to gold nanocolloid solution. Field emission scanning electron microscopy (SEM) image (Figure 2) and surface plasmon resonance (SPR) absorption spectrum (Figure 3) were used to evaluate the size of gold nanoparticles. Near-edge X-ray absorption fine structure (NEXAFS) spectra and X-ray photoelectron spectra (XPS) have been observed at HiSOR BL-13. In the NEXAFS measurements, the incident angle of the soft X-rays was varied from normal (90°) to grazing (40°) incidence with respect to the sample surface.

The size of gold nanoparticles was determined at 7 nm from the SPR peak wavelength shown in Figure 3 based on the analytical equation by Haiss et al [3]. The XPS spectrum of the carbon 1s peak consisted of four peaks, (i) C=C, (ii) H–C–O, C–S–Au, (iii) C=O, and (iv) π–π^* shake off satellite (Figure 4), and the peak intensity ratio (i)/(ii)/(iii) = 5/2/1 was corresponded to the carbon number ratio of MP0. Since the same result was obtained MP0N, it was found that MP0 molecules were densely chemisorbed onto the nanoparticles regardless of their surface shapes.

We have succeeded to observe the polarization dependence of the carbon K-edge NEXAFS spectra of MP0S (Figure 5a, b). From the fitting analysis of the first π^* peak (~285 eV) based on Stohr's analytical formula

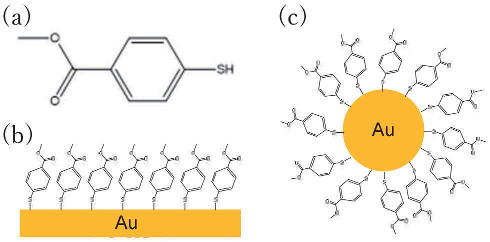

FIGURE 1. (a) Molecular structure of MP0. Schematic drawings of (b) MP0S and (c) MP0N.

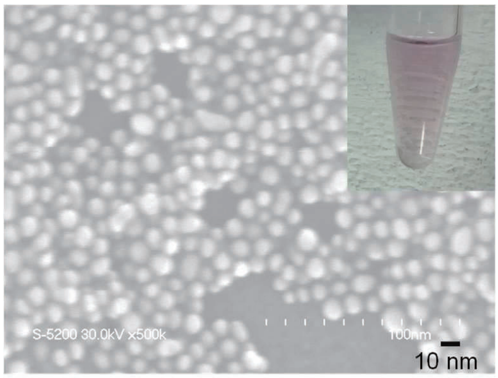

FIGURE 2. SEM image of MP0N. Inset shows the photograph of obtained MP0N nanocolloid solution.

[4], the tilting angle of MP0 molecule from the surface normal have been determined. On the other hand, the polarization dependence of MP0N was not observed in the carbon K-edge NEXAFS spectra (Figure 5c, d), because the gold nanoparticles synthesized in this study were confirmed to be spherical by SEM images (Figure 2). Recently, time-of-flight mass spectrometry was performed at Photon factory BL-2B, and different CH_n^+ ion fragment distribution was obtained between MP0S and MP0N, which are being analyzed from the view point of surface morphology.

REFERENCES

1. B. Corain, G. Schmid and N. Toshima, "Metal Nanoclusters in Catalysis and Materials Science" Amsterdam, Elsevier Science, 2008, pp. 3-4.
2. J. C. Love, L. A. Estroff, J. K. Kriebel, R. G. Nuzzo and G. M. Whitesides, *Chem. Rev* **105**, 2005, pp. 1103-1170.
3. W. Haiss, N. T. K. Thanh, J. Aveyard and D. G. Fernig, *Anal. Chem* **79**, 2007, pp. 4215-4221.
4. J. Stöhr, "NEXAFS spectroscopy" in *Springer Series in Surface Sciences*, edited by R. Gomer., Berlin: Springer, 1992, pp. 284-285.

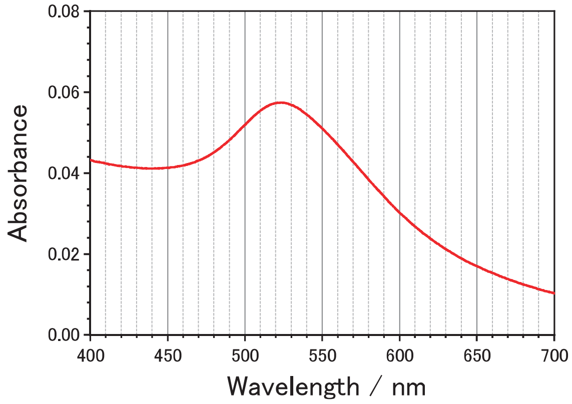

FIGURE 3. Visible spectrum of gold nanocolloid solution. The wavelength of SPR peak was 521 nm.

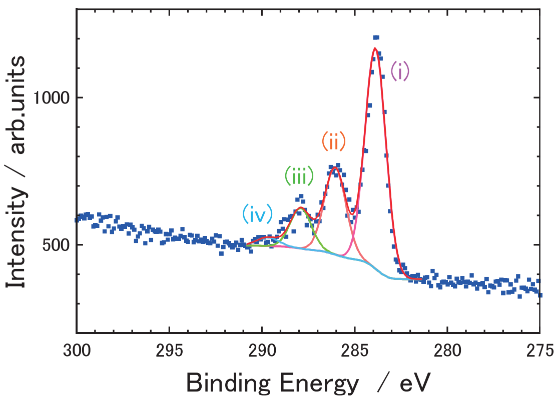

FIGURE 4. Carbon 1s XPS of MP0S.
The four peaks were assigned to (i) C=C, (ii) H–C–O, C–S–Au, (iii) C=O, and (iv) π–π* shake off satellite, respectively.

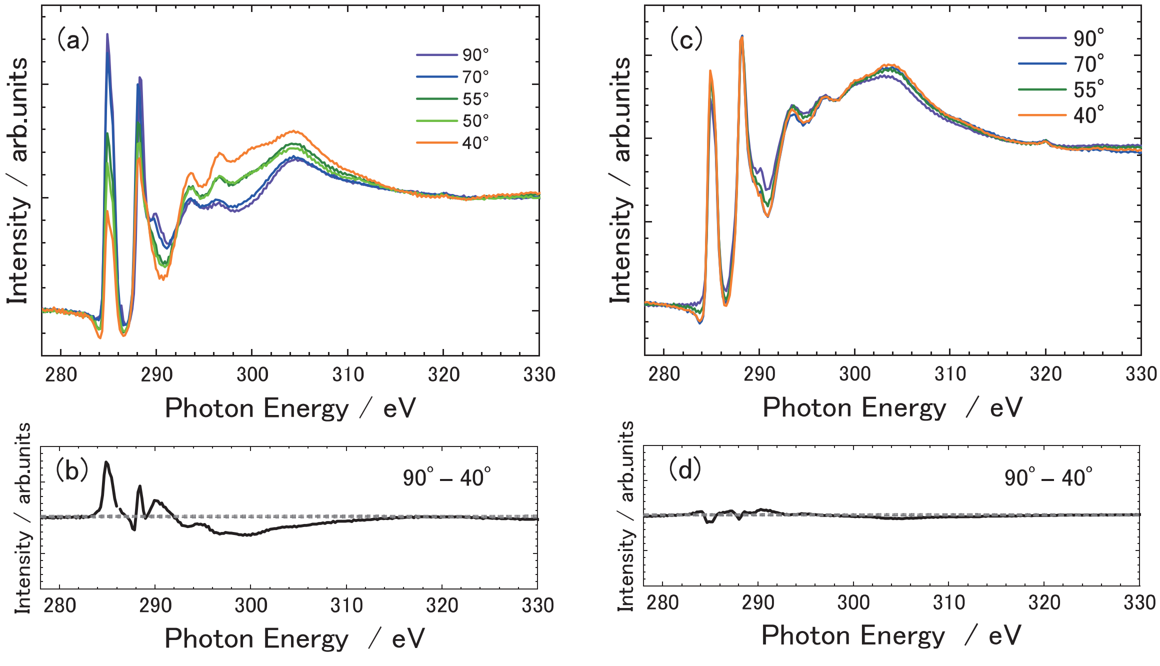

FIGURE 5. Carbon K-edge NEXAFS spectra of (a) MP0S and (c) MP0N, and difference spectra between the normal (90°) and grazing (40°) incidence spectra of (b) MP0S and (d) MP0N. The energy positions of the resonance peaks were consistent between MP0S and MP0N.

20AG038 BL-13

Soft X-ray Polarization Measurement and Evaluation at HiSOR BL-13 Using Electron Orbitally Oriented Samples

Masataka Tabuse[a] and Shin-ichi Wada[a,b]

[a] *Graduate School of Advanced Science and Technology, Hiroshima University*
[b] *Hiroshima Synchrotron Radiation Center, Hiroshima University*

Keywords: NEXAFS, SAMs, HOPG, polarization

Linear polarization is an important parameter for the study of sample orientation and anisotropy of reaction dynamics by X-ray absorption spectroscopy (XAS). Therefore, it is necessary to understand in advance the polarization characteristics of the beamline to be used. Usually, for evaluating the polarization of beamlines, however, it is necessary to insert expensive X-ray polarizers into the beamlines, an ion detection system for anisotropic dissociation induced by polarized SR light, or a photoelectron spectrometer for gaseous molecules.

Recently, the evaluation method of polarization using highly oriented pyrolytic graphite (HOPG), a sample with oriented electron orbitals, was reported [1]. This method makes it possible to easily evaluate polarization by simply rotating the tilted sample in-plane. In this study, the polarization of BL-13 was determined from the dependence on the incidence angle and the validity of the obtained polarization was evaluated by using self-assembled monolayers (SAMs).

HOPG is a solid sample with highly oriented electron orbitals that can maintain its planarity, and it was fixed on a sample stand with an tilted angle of 30° (Fig. 1). In a typical sample arrangement, only the horizontal component of the electric field vector can be evaluated.

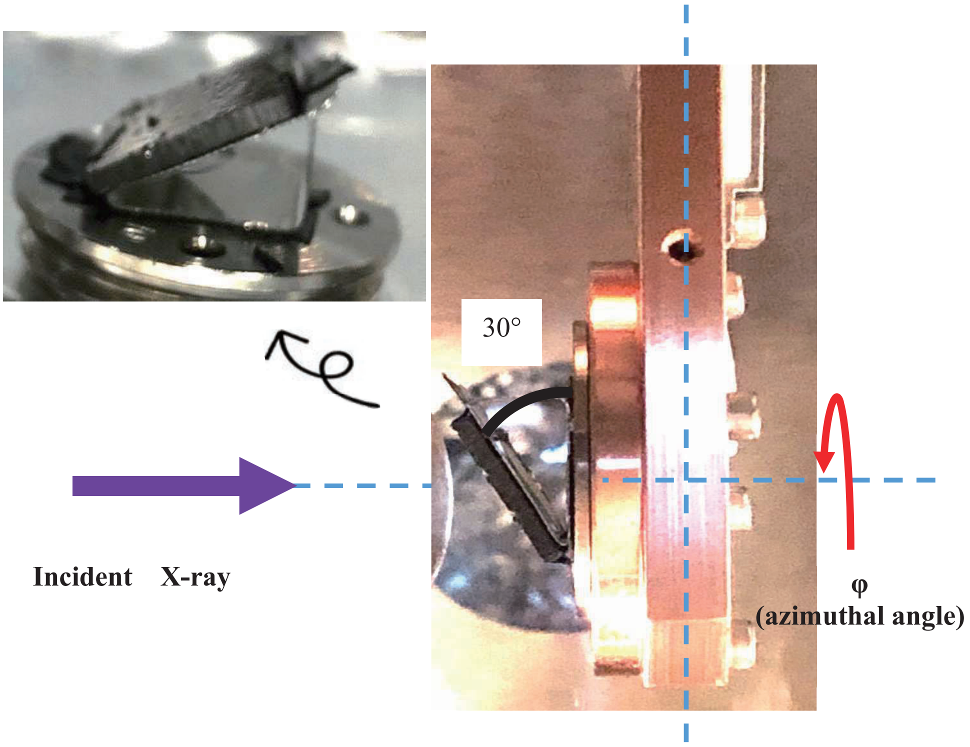

FIGURE 1. Photos of the tilted HOPG sample introduced to BL-13.

The angle dependence of the X-ray absorption fine structure (NEXAFS) spectra was measured at various azimuthal angles (φ) as shown in Fig. 2. The intensity of the π*(C=C) transition peak at 285 eV increases as the azimuth angle increases. On the contrary, the intensity of the peak from the σ*(C=C) transition around 292eV to around 312eV and 330eV decreases as the azimuth angle is increased. The polarization of BL-13 was determined from the analysis of such angle dependence.

The obtained result was applied to the determination of the orientation angle of alkanethiol SAMs with respect to the gold substrate (Fig. 3) and the obtained orientation angles were compared with the literature values. In addition, biomembranes prepared only by dropping lipid solution onto substrates was also evaluated by polarized SR light. The spectra showed clear polarization dependence, indicating the layered conformation of biomembranes formed by such simple method.

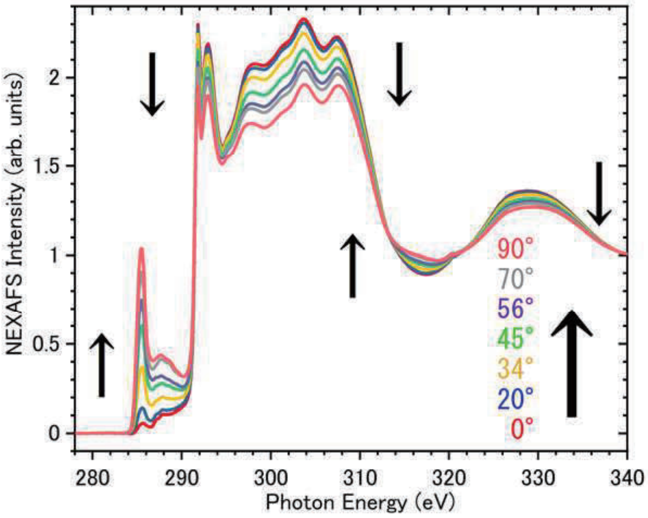

FIGURE 2. Azimuthal angle dependence of NEXAFS spectra of HOPG.

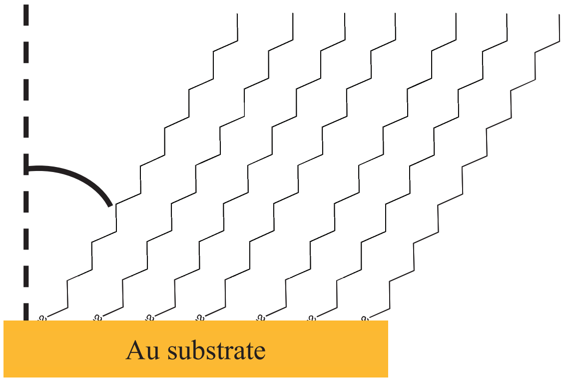

FIGURE 3. Schematic diagram of SAMs.

REFERENCES

1. B. Watts, L. Thomsen and P.C. Dastoor, J. Electron Spectrosc. Relat. Phenom. 151 (2006) 208.

X-ray Absorption Spectroscopy of Self-assembled Monolayers Prepared on a Thin Gold Wire

Yasumasa Hikosaka[a] and Shin-ichi Wada[b]

[a]*University of Toyama, 2630 Sugitani, Toyama, 930-0194, Japan*
[b]*Hiroshima University, 1-3-1 Kagamiyama, Higashi-Hiroshima, 739-8526 Japan*

Keywords: X-ray photoelectron spectroscopy; X-ray absorption spectroscopy; Self-assembled monolayers.

Self-assembled monolayers (SAMs) with methyl ester groups exhibit extremely high site-selective bond cleavages upon soft X-ray irradiation [1]. To gain insight into the promoting mechanism, we plan to investigate the decay pathways of the inner-shell vacancies created in SAM by soft X-ray absorption, by using an electron coincidence method with a magnetic bottle electron spectrometer. It is known that a solid sample can be targeted by the electron coincidence method, when it is condensed on a thin wire [2].

In this study, we have examined the appropriate preparation of a methyl 16-mercaptohexadecanoate (MHDA) SAM on the surface of a thin wire, by X-ray absorption spectroscopy. MHDA-SAM has an end functional group of methyl-ester terminated aliphatic thiol, which is the same as the methyl ester functional group contained in a poly(methyl methacrylate) (PMMA) thin film whose site-selective bond cleavages have also been extensively studied [1]. A thin gold wire (0.3-mm diameter) was repeatedly washed with ethanol and acetone, and then was immersed into an ethanol solution of MHDA. Figure 1 shows the total electron yield spectra measured for the wire in the carbon 1s and oxygen 1s regions. The spectral profiles seen in Fig. 1 are in general agreement with those in the spectra for SAMs fabricated on gold-coated Si plates [3], and the assignments given for the remarkable structures are indicated in the figures. It is known that the core-to-valence transitions in the MHDA-SAM fabricated on a plate show clear dependences on the incidence angle of soft x-ray to the surface [3]. For example, the structure due to the C1s → σ*(C-C) excitation is enhanced as decreasing the incidence angle, while the C1s → σ*(C=O) structure shows an opposite trend. For the present MHDA-SAM sample prepared on a wire, the angle of incident light is not particularly defined. The spectral profiles seen in Fig. 1 are reasonable as the integration of the spectra of different incidence angles. It is thus confirmed by the present X-ray absorption spectroscopic measurement that an MHDA film of single monolayer size was indeed formed on the surface of a thin gold wire. However, compared to the spectra in the literature [3], an extra structure is observed in Fig. 1(a) at a photon energy of 285 eV. This observation may suggest that carbon contamination to the surface of the prepared sample, but it could also be an artifact caused by a rapid change in the light intensity in this photon energy region due to the carbon contamination to the beamline mirrors. We are conducting further research on the sample preparation and evaluation methods.

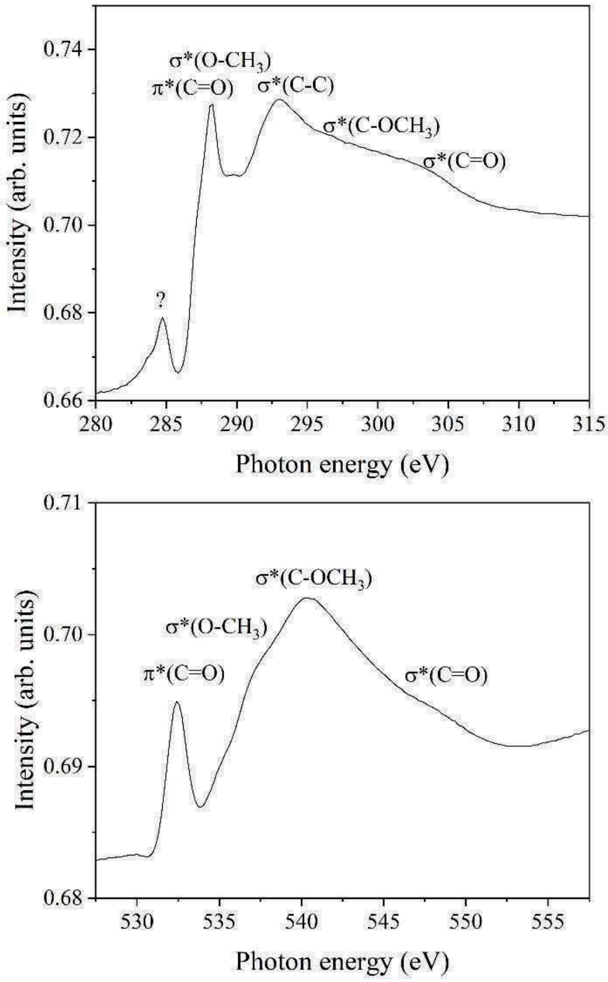

FIGURE 1. Total electron yield spectra measured for the MHDA-SAM sample prepared on a thin gold wire in (a) the carbon 1s and (b) oxygen 1s regions.

REFERENCES

1. S. Wada et al., *J. Phys.: Condens. Matter* **18**, S1629 (2006).
2. Y. Hikosaka et al., J Electron Spectrosc. Rel. Phenom. **213**, 17–21 (2016).
3. S. Wada et al., *Sur. Sci.* **593**, 283-290 (2005).

Growth mode and interface structure of Co ultrathin films evaporated on h-BN/Ni(111)

Wataru Nishizawa[a] , Tatsuya Mayumi[c], Masahiro Sawada[c]

[a] Department of Physics, School of Science, Hiroshima University
[b] Graduate School of Science, Hiroshima University
[c] Hiroshima Synchrotron Radiation Center, Hiroshima University

Keywords: epitaxial growth, hexagonal boron nitride, Auger electron spectroscopy

Magnetic tunneling junction (MTJ) structures, where ferromagnetic electrode layers sandwich an insulating barrier layer, show tunnel magnetic resistance (TMR) effect that is widely applied for spintronics devices such as magnetic random access memory. One of important performance factors of TMR element is magnetic resistance (MR) ratio, which is sensitive to not only electronic and magnetic status in the magnetic electrode layers but also the interface structure between the barrier layer and each magnetic layer. Conventionally, metal oxide layers like aluminum oxide have been utilized for the barrier layer in the device structures, where improvement of MR ratio is limited because of disorder of crystal structures at the interface, arises from lattice mismatch, inter-diffusion or defect inclusion. In recent years, much attention and intensive studies have been devoted to hexagonal boron nitride (h-BN) whose structure is composed of two dimensional honeycomb layers formed by stable chemical bonding. Monolayer h-BN is one of good candidates for the ideal burrier layer of TMR devices because the h-BN layer is expected to form a sharp and abrupt interface without pinhole defects with typical magnetic elements. A ultrathin MTJ structure of Co/h-BN/Ni(111) is also considered to form ideal interface from good lattice matching between the h-BN layer and magnetic transition metals. Although the commensurate interface of h-BN/Ni(111) is well established by previous studies, the growth mode and interface structure for Co/h-BN has not been clarified as yet.

In this study, we have investigated growth mode of Co films on h-BN/Ni(111) in manner of quantitative analysis of Auger electron intensity that is depending on Co thickness in several monolayer region. The sample of Co/h-BN/Ni(111) was prepared in ultra-high vacuum by means of MBE evaporation of Co on h-BN/Ni(111), where high quality h-BN monolayer was fabricated on the clean surface of Ni(111) by cracking of borazine ($B_3N_3H_6$) [1]. Figure 1 shows intensity ratio of Co (LMM) to Ni (LMM) in Auger electron spectra (AES), whose thickness dependence is clearly revealed. Simple exponential expansion of Co signal has not found from data fitting analysis, leading to a failure of complete layer-by-layer growth. We can suggest initial islanding growth followed by two dimensional epitaxial growth above 4 ML.

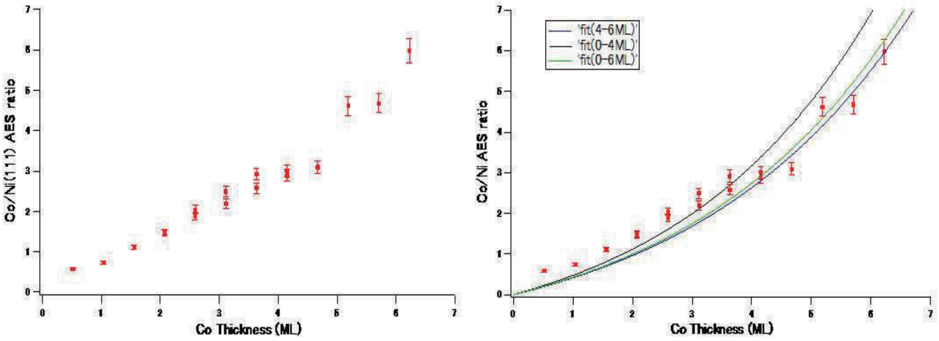

FIGURE 1. Co thickness dependence of intensity ratio of Auger electron of Co (LMM) to Ni (LMM) obtained from differential Auger electron spectra from Co/h-BN/Ni(111). Some of fitting models are also shown on the right panel.

REFERENCES

1. A. Nagashima *et al.*, Phys. Rev. B51, 4606 (1995).